SATEBAL: A Semi-Passive Orbital Attitude Stabilization System Using a Controllable Deployment Mechanism

Yan-Siou Liu, Chao-Hsien Chih, Yu-Hsin Chen, Yu-Hsiang Chen,
Pin-Yun Li, Tzu-Ching Su, Chih-Yu Lin, Ai-Lin Liu
Advisers: Woei-Leong Chan, Yu-Jui Liang
Institute of Space Systems Engineering,
Department of Aeronautics and Astronautics,
and International Bachelor Degree Program on Energy Engineering
National Cheng Kung University (NCKU)
Tainan, Taiwan

Abstract

This paper presents SATEBAL, a CubeSat mission designed to demonstrate a semi-passive orbital attitude stabilization and deorbiting strategy integrating a controllable deployment mechanism. The system consists of two main phases: passive attitude control using deployable booms with tip masses and accelerated orbital decay via a deployable drag sail. In the first phase, the CubeSat's mass distribution on the booms is adaptively tuned to passively stabilize its orientation under gravity gradient torque by optimizing the principal moments of inertia. A FreeRTOS-based OBDH system enables precise real-time coordination of control tasks. In the second phase, a cross-shaped Mylar sail is deployed to enhance atmospheric drag, ensuring the satellite reenters within 70 days, as verified by STK simulations. Aerodynamic modeling, using Free Molecular Flow and Response Surface Methodology, validates drag coefficients under varying flow conditions. A hybrid ADCS combining passive and magnetorquer-based active control is proposed, with Lyapunov-based stability guarantees under external disturbances. Structural and thermal analyses confirm mission viability. This mission provides a compact, energy-efficient platform for attitude control and post-mission disposal, supporting future CubeSat designs aiming for agility and sustainability in low Earth orbit operations.

1. Mission concept and objectives

SATEBAL is a CubeSat mission that demonstrates passive deorbiting using a deployable drag sail and boom-based attitude control. SATEBAL includes two parts of the mission, which is shown in Figure 1. At first, upon reaching orbit, the CubeSat extends four lightweight booms with tip masses, allowing it to passively align using gravity gradient torque by adjusting its inertia distribution. This energy-efficient method enables the satellite to achieve and maintain a desired attitude without relying on continuous active control. After the phase one mission is completed, part 2 mission will begin. A deployable drag sail is released to increase the satellite's cross-sectional area, enhancing interaction with the rarefied upper atmosphere. The mission validates aerodynamic drag coefficients in rarefied flow and showcases a hybrid ADCS approach, supporting future small satellite missions with energy-efficient stabilization and compliant space debris mitigation.

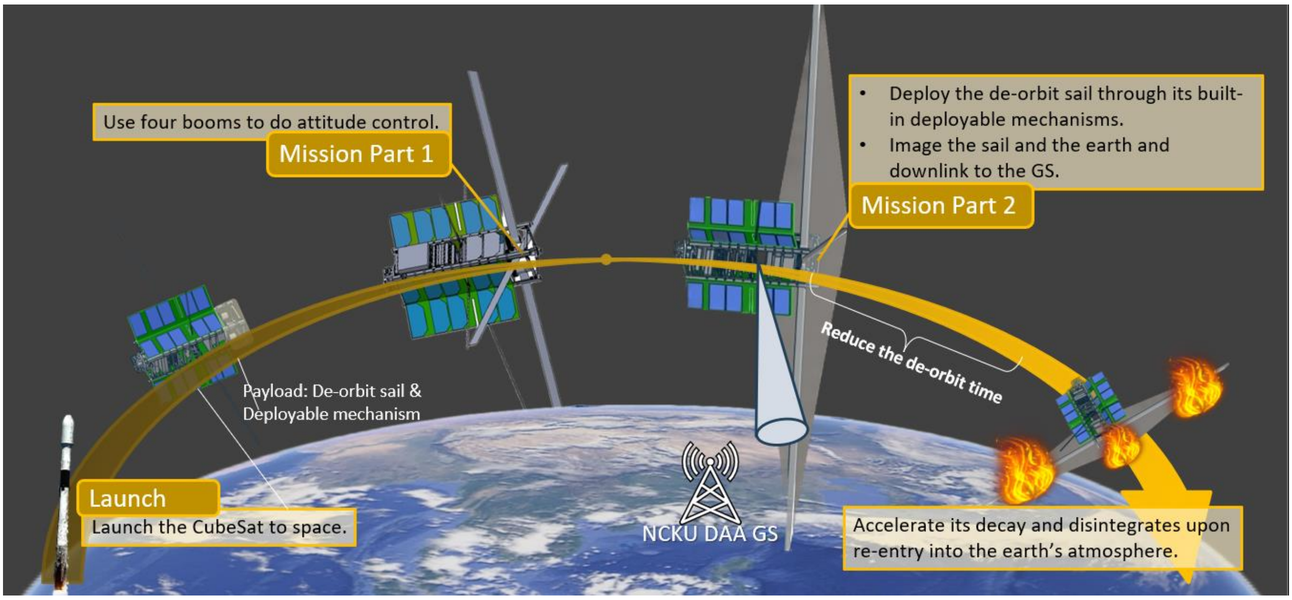

Figure 1 The mission concept of SATEBAL

In part 1 mission, attitude stabilization is a fundamental requirement for satellite operations. Over the decades, passive attitude stabilization systems have been widely adopted in low earth orbit satellites due to their simplicity, reliability, and low power consumption. Among the various passive stabilization strategies, gravity gradient torque (Fischell & Mobley, 1964), aerodynamic torque (Bak & Wisniewski, 1997; Kumar et al., 1995), and geomagnetic torque (Fiorillo et al., 2010) are commonly utilized for attitude stabilization. These environmental torques enable attitude stabilization in low earth orbit without relying on active control, providing an efficient and robust solution for maintaining the desired orientation (Psiaki, 2004). While this approach is energy-efficient and offers a long operational lifespan, it often falls short in providing the agility needed for flexible or rapid attitude adjustments.

To overcome these limitations, hybrid stabilization strategies that combine passive elements with deployable mechanisms and active control have been proposed. This deployable attitude stabilization system is a novel configuration consisting of four extendable rods, each equipped with a tip mass. By adjusting the length of these rods, the overall mass distribution of the satellite can be changed, thereby modifying the principal moments of inertia. By modulating the inertia tensor, the system can achieve various equilibrium orientations when subjected to gravity gradient torque. In particular, the satellite can be passively guided toward a desired attitude equilibrium by tuning the inertia distribution such that the gravity gradient torque naturally drives the system to a target configuration. By taking advantage of naturally occurring environmental torques, this strategy allows for equilibrium modulation without necessitating continuous actuation.

The deployable attitude stabilization mechanism is governed by an optimization process, as illustrated in Figure 2. The procedure begins with determining the desired satellite attitude based on mission requirements, such as nadir pointing or alignment with the sun vector. Using the nadir and orbital normal vectors, a target attitude matrix is constructed, from which a desired set of principal axes (eigenvectors) is derived. To achieve this desired configuration, a constrained optimization problem is formulated to compute the appropriate lengths of the four deployable rods, each with a tip mass. The objective is to modify the satellite's inertia matrix so that it aligns with the target eigenvectors, ensuring passive convergence under gravity gradient torque. Once the optimal rod lengths are obtained, they are transmitted to the satellite via the TT&C subsystem, enabling the adjustment of the satellite's physical configuration in orbit.

To support this deployable mechanism, a hybrid attitude determination and feedback control system is implemented, as shown in Figure 3. The close loop system comprises an attitude and heading reference system (AHRS) and sensors for real-time state estimation, a controller that generates control torque command, and magnetorquers serving as actuators. This closed-loop architecture allows the system to respond to external disturbances and maintain precise pointing. When deviations from the desired attitude occur, the controller engages the magnetorquers to apply corrective torques, while the passive deployable system gradually steers the satellite toward a new equilibrium by modulating the inertia distribution. This hybrid approach provides both energy-efficient long-term stabilization and the agility required for mission-specific pointing requirements.

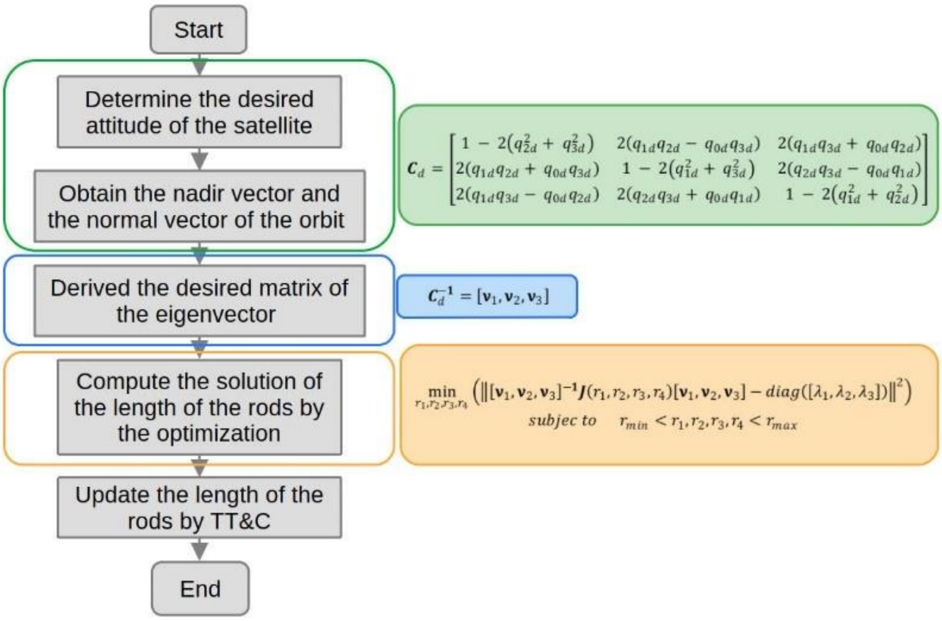

Figure 2 Illustration of the workflow to determine the command of the deployment system.

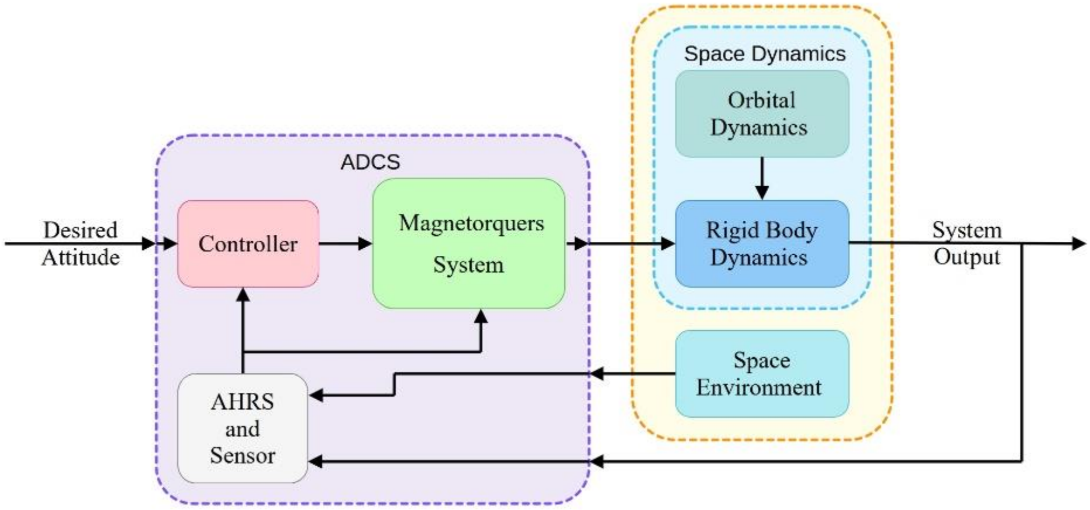

Figure 3 The block diagram of the satellite close loop control.

In part 2 mission, SATEBAL draws inspiration from notable solar and drag sail missions such as LightSail 2 (Spencer et al., 2021) and NASA's Advanced Composite Solar Sail System (ACS3) (Wilkie, 2021), both of which demonstrated the feasibility of deploying large, lightweight surfaces in space to manipulate orbital dynamics. While LightSail 2 achieved controlled orbit raising via solar radiation pressure, the SATEBAL mission focuses on accelerating orbital decay for deorbiting purposes. The self-deployable drag sail enables SATEBAL to serve as a technology demonstrator for passive deorbiting strategies, aligning with international guidelines for space debris mitigation such as those recommended by the Inter-Agency Space Debris Coordination Committee (Yakovlev, 2005). By ensuring that the spacecraft reenters Earth’s atmosphere within an acceptable post-mission timeframe, the drag sail reduces the risk of contributing to the growing problem of orbital debris.

SATEBAL demonstrates the integration of deployable structures with attitude control and deploy the drag sail to deorbit. A key innovation of the mission is the automated system that combines a variable-size drag sail with a boom-based attitude control mechanism. This configuration allows the satellite to adjust its aerodynamic cross-section and orientation in real time, improving the effectiveness and precision of the deorbiting process. The system enhances control during orbital decay by coordinating aerodynamic forces with passive stabilization. The integration of deployable elements with attitude control also serves as a foundation for more advanced hybrid systems that combine environmental torques with shape-adaptive configurations for future agile satellite missions. The following sections provide a detailed overview of the mission’s key parameters and orbital analysis, including altitude selection, expected decay behavior, and aerodynamic modeling. Each subsystem—attitude determination and control, power, communications, structure, and thermal design—is then examined to assess the integration, functionality, and overall performance of the satellite in achieving its mission objectives.

2. Mission Requirements

Phase	Requirement content
Phase 0: Satellite Deployment	
REQ.1	SATEBAL shall start to collect housekeeping data and broadcast Beacon automatically after 30 minutes from the deployment from the deployer, and also deploy UHF/VHF antennas.
Phase 1: Initial Commissioning	
REQ.2	Functionality of OBC shall be fully checked, and make sure the normal data read/write/delete functionality.
REQ.3	Overall system functionality shall be checked for normal performance.
Phase 2: ADCS Operation	
REQ.4	SATEBAL shall be detumbled and controlled to desired attitude via the ground command. Attitude Velocity: $\omega \leq 5°/s$
REQ.5	Make sure the side panels are deployed normally.

REQ.6	SATEBAL shall be stabilized in desired attitude after side panels deployment. Pointing Error: $e \leq 1°$
Phase 3: Payload Camera Commissioning	
REQ.7	The Cameras shall be checked for image acquisition and downloading
Phase 4: Payload Deployed Sail Demonstration	
REQ.8	The sail shall be deployed from the SATEBAL.
REQ.9	SATEBAL's attitude shall be stabilized during the sail deployment.
REQ.10	Images of the deployed sail shall be captured and downloaded. Its deployment shall be quantified.
REQ.11	The position data shall be accurately obtained and downloaded as SATEBAL decays and re-enters.
REQ.12	Aerodynamic characteristics of deployed sail, derived from the position and velocity data, shall be recorded and downloaded.
End: End of Lifetime	
REQ.13	SATEBAL shall terminate signal broadcast on all frequency spectrum, if the mission is more than 5 years.
* REQ: Requirement	

3. Key parameters of mission

3.1Payload- Deployed sail and Deployable mechanism

This project introduces SATEBAL, a CubeSat mission developed to demonstrate an efficient, compact deorbiting mechanism based on aerodynamic drag enhancement. In response to the increasing threat of orbital debris, SATEBAL aims to provide a cost-effective and lightweight solution that passively accelerates orbital decay at the end of a CubeSat's operational life. The payload integrates a deployable drag sail system fully stowed within a standard 1U volume, allowing seamless integration with existing CubeSat buses. Upon command, the sail deploys to dramatically increase the satellite's surface area exposed to atmospheric particles in low Earth orbit (LEO), thereby enhancing drag and expediting atmospheric re-entry. This passive approach supports compliance with space debris mitigation guidelines, contributing to sustainable and responsible orbital operations.

3.1.1 Deployable Sail and Structural Layout

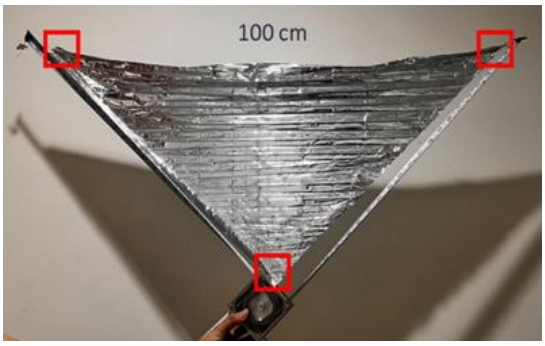

Figure 4
Schematic of single solar sail deployment

Figure 5
Full-array deployment of the solar sail system

At the core of the deorbiting system is a cross-shaped sail assembly, consisting of four ultra-thin triangular Mylar sails, each just 4.6 μm thick. These sails are symmetrically arranged to span an effective 1-meter side length, achieving a total deployed area of 1 square meter. Each triangular sail is anchored at its base to the satellite body and tensioned outward by a corresponding composite boom, allowing for even force distribution and balanced aerodynamic response. The design draws direct inspiration from the LightSail 2 (The Planetary Society, 2019) and ACS3 (Wilkie et al., 2021) missions, but has been optimized for tighter volume constraints and better structural stability during and after deployment.

Mylar was selected as the sail material due to its outstanding characteristics:

1. Lightweight and low volume, ideal for CubeSat payload restrictions
2. High tensile strength and tear resistance, ensuring reliable unfolding
3. Radiation and thermal resistance, supporting durability in LEO
4. Flight-proven heritage in solar sails, thermal insulation, and sounding balloon envelopes

These properties ensure that the sails can be densely folded, stowed, and redeployed without significant degradation over time or through multiple thermal cycles in space.

3.1.2 Four-Boom Controlled Deployment System

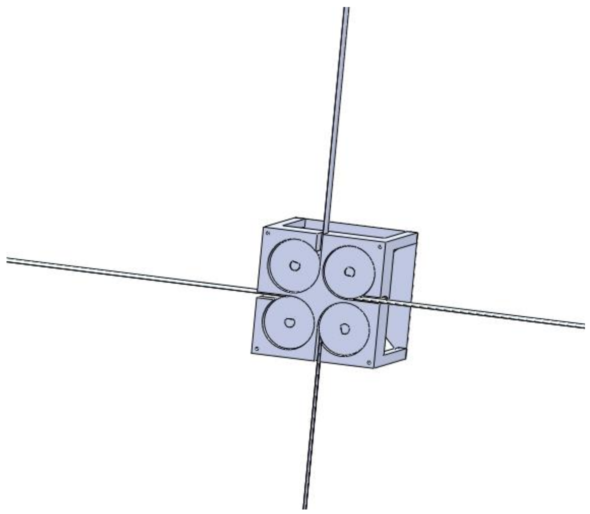

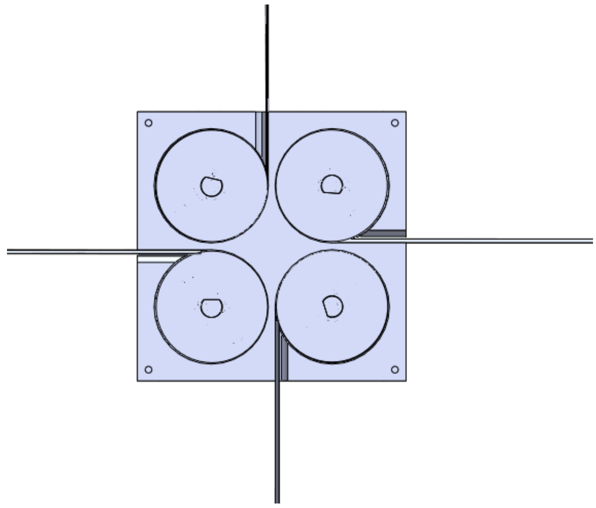

Figure 5 Payload structure **Figure 7** Top view of payload structure

Sail deployment is achieved through a four-boom controlled extension mechanism, where each sail edge is independently tensioned by its own boom. The booms are made of C-shaped laminated carbon fiber composites, performed using prepreg layups and cured for high stiffness-to-weight performance. These booms are coiled in a preloaded state and stowed within the CubeSat body. Upon deployment, each boom is gradually unspooled to pull its corresponding sail outward, forming the complete cross-sail geometry.

To ensure controlled and reliable deployment, a motor-actuated mechanism governs the extension of each boom. While the composite booms possess natural strain energy for self-expansion, motors are used to regulate speed, sequence, and symmetry, preventing abrupt movements or entanglement. This is critical not only for successful geometric formation, but also for maintaining SATEBAL's attitude stability during the deployment phase.

Each motor unit is coupled with a gear-reduction system and feedback sensor for precise actuation, allowing deployment to be monitored and halted in the event of anomalies. The architecture ensures that sail tension is properly distributed across all four arms, minimizing wrinkling or asymmetry that could reduce drag efficiency or affect attitude control. In its fully deployed configuration, the drag area is maximized, and the satellite enters a passively stable aerodynamic state, accelerating orbital decay in accordance with post-mission disposal protocols.

3.1.3 Micro Metal Gear Motor for Payload Deployment Mechanism (GA12-N20)

The payload deployment mechanism employs GA12-N20 micro metal gear motors as the primary actuators. These compact, durable DC gear motors support PWM speed control, making them well-suited for the confined space of a CubeSat. Each motor has a 12 mm outer diameter, a 3 mm output shaft diameter, and a 10 mm shaft length. The nominal operating voltage is 6 V, with a functional range of 3–12 V, allowing flexible power management within the satellite's electrical subsystem.

At 12 V, the GA12-N20 achieves a no-load speed of 100 rpm and a loaded speed of 80 rpm, delivering a rated torque of 2 kg·cm and a stall torque up to 16 kg·cm. The corresponding current draw is approximately 150 mA under load and 300 mA at stall. Its 298:1 metal gearbox provides high torque output, excellent wear resistance, and sufficient mechanical advantage to overcome the initial resistance during boom deployment and sail unfolding.

Although the initial release of the booms is triggered by a burn-wire mechanism, the GA12-N20 motors play a critical role in regulating deployment speed and adjusting post-deployment tension. This configuration ensures smooth and symmetrical extension, minimizes the risk of entanglement, and supports the satellite's semi-passive attitude stabilization and controlled deorbiting objectives.

3.1.4 Structural and Environmental Simulation Analysis

Prior to physical integration, a series of numerical simulations were conducted to evaluate the mechanical robustness and environmental survivability of the deployable deorbiting system. Using ANSYS Workbench, the CubeSat structure underwent modal analysis to determine its natural frequencies and avoid resonance with launch-induced vibration profiles. The results confirmed sufficient margin between the structure's dominant modes and typical launch spectra, mitigating the risk of fatigue or mechanical failure.

To assess environmental tolerance, a steady-state thermal simulation was performed, modeling orbital temperature variations from −40°C to +80°C. Material properties of Mylar sails and carbon composite booms were validated to remain within safe stress and deformation limits under these thermal extremes. Additionally, a preliminary drag force estimation was conducted using orbital decay models, suggesting that the fully deployed 1 m^2 sail can reduce orbital lifetime from several years to less than 18 months at an altitude of ~600 km. These analyses support the mechanical and functional viability of the system for real-space deployment conditions, laying the groundwork for subsequent environmental testing and qualification.

3.1.5 Integration, Testing, and Flight Readiness

Following the completion of the conceptual and structural design, the deorbiting mechanism progressed to prototype-level integration and ground-based functional testing, achieving a Technology Readiness Level (TRL) of 4. Each Mylar sail was precision-cut and reinforced at key stress points using eyelets and transparent tape, ensuring reliable unfolding and tear resistance. The composite booms were assembled onto custom dual-hole mounts, with tension carefully adjusted using fishing-line guides to prevent misalignment during deployment.

A series of manual and motor-assisted deployment tests were conducted in ambient laboratory conditions to verify sail expansion geometry and boom kinematics. The motors successfully actuated all four booms individually, with limit switches confirming the full extension of each arm. Additionally, electrical testing verified that the motor driver circuitry operates within acceptable voltage and current margins. These integration efforts confirmed that the structure can be stowed, deployed, and reset repeatedly without mechanical failure.

3.2 Attitude Determination and Control System (ADCS)

This section primarily addresses a detailed formulation of the satellite's flight dynamics. Following the development of the dynamic model, the design of the ADCS is introduced. The deployable attitude stabilization system is introduced and modeled to enhance the stability of the attitude of the satellite. Moreover, a stability analysis of the proposed control system is conducted to ensure robust performance under realistic operating conditions.

The hardware selected for this task is the ADCS-MTQ developed by Tensor Tech. Figure   is the picture of the ADCS-MTQ, and the technical specifications is listed in Table 1.

Figure 7 The ADCS-MTQ developed by Tensor Tech.

Table 1 The technical specifications.

ADCS-MTQ	
mass	**207 g**
volume	**0.2 U**
supply voltage	**3.3 V or 5 V**
power consumption	**< 1 W**
magnetic dipole moment	**< 0.2 A m^2**
pointing knowledge	**0.3 deg**
angular control accuracy	**5 deg**

3.2.1 Dynamic Modeling

The low earth circular orbit is considered. There are two reference frames to be used to describe the motion of the satellite in Figure 8 and Figure 9. The local vertical local horizontal (LVLH) reference frame, denoted as $\mathcal{G}x_o y_o z_o$, is defined to describe the gravity vector. The body frame, denoted as $\mathcal{B}xyz$, is utilized to describe the rotation motion. The orientation, or namely attitude, can be expressed as a direction cosine matrix (DCM), denoted as $\mathbf{C}$. The attitude dynamic equation is

$$\mathbf{C}=\mathbf{C}\boldsymbol{\omega}\times \tag{1}$$

where $\boldsymbol{\omega} = \left[\omega_x, \omega_y, \omega_z\right]^T$ is the angular velocity vector, $[\cdot]^\times$ denotes the cross-product matrix, and the rotational dynamic equation of the satellite can be given

$$\mathbf{J}\dot{\boldsymbol{\omega}} + [\boldsymbol{\omega}]^\times \mathbf{J}\boldsymbol{\omega} - \mathbf{L}_G - \boldsymbol{\tau}_c - \boldsymbol{\tau}_d = 0 \tag{2}$$

here $\mathbf{J}$ is the moment of inertia, $\boldsymbol{\tau}_c$ is the control torque generated by the magnetorquers, $\boldsymbol{\tau}_d$ is the external disturbance torque induced by the aerodynamics and solar pressure, $\mathbf{L}_G$ is the gravity gradient torque

$$\mathbf{L}_G = \mu[\hat{n}]^\times J\hat{n}, \qquad \mu = \frac{3\mathrm{GM_e}}{R^3} \tag{3}$$

and G is gravitational constant, M_e is the mass of earth, $\hat{n}$ is the nadir pointing vector can be described by the DCM

$$\hat{n} = \mathbf{C}^T \hat{z}_o \tag{4}$$

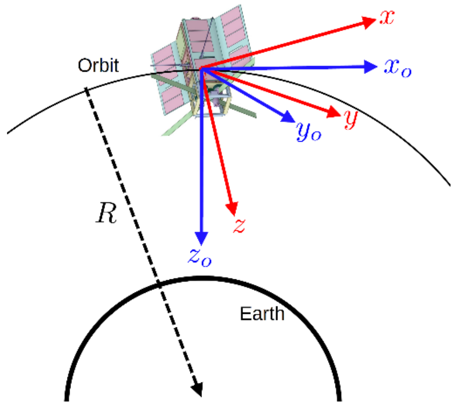

Figure 8 Illustration of the coordinate system of satellite.

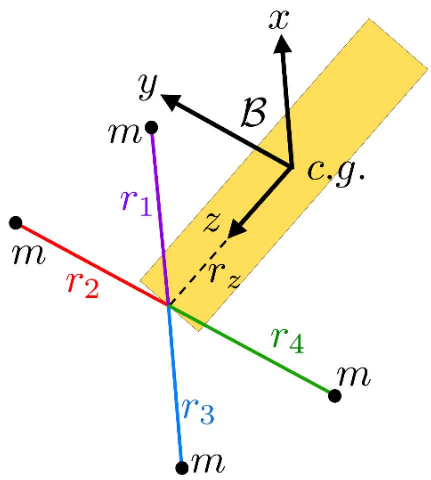

Figure 9 Illustration of the attitude stabilization system.

3.2.2 Principal axes of the Inertia Matrix

The geometry of the stabilization system is shown in Figure . There are four moveable masses m connected by the roads. The length of the rods is denoted as r_1, r_2, r_3 and r_4. The inertia matrix of the satellite can be calculated by

$$\mathbf{J} = \mathbf{J}_s + \mathbf{J}_1 + \mathbf{J}_2 + \mathbf{J}_3 + \mathbf{J}_4 \tag{5}$$

where J_s is the inertia matrix of 3U CubeSat excluding deployable components, the inertia matrix of the deployable components can be given by

$$\mathbf{J}_1 = \begin{bmatrix} 0 & 0 & -r_1 r_z \\ 0 & r_1^2 & 0 \\ -r_1 r_z & 0 & r_1^2 \end{bmatrix} + \begin{bmatrix} r_z^2 & 0 & 0 \\ 0 & r_z^2 & 0 \\ 0 & 0 & 0 \end{bmatrix} \tag{6}$$

$$\mathbf{J}_2 = \begin{bmatrix} r_2^2 & 0 & 0 \\ 0 & 0 & -r_2 r_z \\ 0 & -r_2 r_z & r_2^2 \end{bmatrix} + \begin{bmatrix} r_z^2 & 0 & 0 \\ 0 & r_z^2 & 0 \\ 0 & 0 & 0 \end{bmatrix} \tag{7}$$

$$\mathbf{J}_3 = \begin{bmatrix} 0 & 0 & r_3 r_z \\ 0 & r_3^2 & 0 \\ r_3 r_z & 0 & r_3^2 \end{bmatrix} + \begin{bmatrix} r_z^2 & 0 & 0 \\ 0 & r_z^2 & 0 \\ 0 & 0 & 0 \end{bmatrix} \tag{8}$$

$$\mathbf{J}_1 = \begin{bmatrix} r_4^2 & 0 & 0 \\ 0 & 0 & r_4 r_z \\ 0 & r_4 r_z & r_4^2 \end{bmatrix} + \begin{bmatrix} r_z^2 & 0 & 0 \\ 0 & r_z^2 & 0 \\ 0 & 0 & 0 \end{bmatrix} \tag{9}$$

According to the preliminary research [8], the following theorem has been proven

Theorem 1. *The equilibrium point of gravity gradient stabilization is determined about the eigenvalue and the eigenvector of the inertia matrix* $\mathbf{J}$. *The sufficient conditions for three-axis stabilization is*

$$\lambda_3 < \lambda_2 < \lambda_1 \tag{10}$$

where λ_1 *is the maximum eigenvalue with the corresponding eigenvector* $\mathbf{v}_1$, λ_2 *is the middle eigenvalue with the corresponding eigenvector* $\mathbf{v}_2$, λ_3 *is the minimum eigenvalue with the* *corresponding eigenvector* $\mathbf{v}_3$*. In the Lyapunov sense, the satellite attitude is considered stable when its smallest inertia axis* $\mathbf{v}_3$ *points toward the Earth (nadir direction), while its largest inertia axis* $\mathbf{v}_1$ *is perpendicular to the orbital plane.*

Thus, the system is designed so that the principal axes of inertia coincide with the target attitude, enabling passive stabilization. The diagonalization of the inertia J can be designed as

$$[\mathbf{v}_1, \mathbf{v}_2, \mathbf{v}_3]^{-1}\mathbf{J}[\mathbf{v}_1, \mathbf{v}_2, \mathbf{v}_3] = diag([\lambda_1, \lambda_2, \lambda_3]) \tag{11}$$

That is, the equilibrium point of the attitude can be guaranteed by designing the eigenvector of the inertia matrix, the desired orientation $\boldsymbol{C}_d^{-1}$ can be represented as

$$\mathbf{C}_d^{-1} = [\mathbf{v}_1, \mathbf{v}_2, \mathbf{v}_3] \tag{12}$$

According to the transformation relationship of the quaternion and DCM, the eigenvector and be derived by the desired quaternion $\boldsymbol{q}_d = [q_{0d}, q_{1d}, q_{2d}, q_{3d}]$:

$$\mathbf{C}_d = \begin{bmatrix} 1 - 2(q_{2d}^2 + q_{3d}^2) & 2(q_{1d}q_{2d} - q_{0d}q_{3d}) & 2(q_{1d}q_{3d} + q_{0d}q_{2d}) \\ 2(q_{1d}q_{2d} + q_{0d}q_{3d}) & 1 - 2(q_{1d}^2 + q_{3d}^2) & 2(q_{2d}q_{3d} - q_{0d}q_{1d}) \\ 2(q_{1d}q_{3d} - q_{0d}q_{2d}) & 2(q_{2d}q_{3d} + q_{0d}q_{1d}) & 1 - 2(q_{1d}^2 + q_{2d}^2) \end{bmatrix} \tag{13}$$

Thus, the corresponding length of the rods can be computed by solving an optimization problem to modify the inertia matrix with the desired eigenvector

$$\begin{gathered} \min_{r_1, r_2, r_3, r_4} \left(\left\| [\mathbf{v}_1, \mathbf{v}_2, \mathbf{v}_3]^{-1}\mathbf{J}(r_1, r_2, r_3, r_4)[\mathbf{v}_1, \mathbf{v}_2, \mathbf{v}_3] - diag([\lambda_1, \lambda_2, \lambda_3]) \right\|^2 \right) \\ subjec\ to \quad r_{min} < r_1, r_2, r_3, r_4 < r_{max} \end{gathered} \tag{14}$$

where r_{min} and r_{max} are the minimum and maximum of the length of robs, respectively.

Figure describes the methodology workflow to determine the length of the rods. So far, the deployment system has been designed to stabilize the satellite attitude without the active control system.

3.2.3 Controller Design and Stability Analysis

Nevertheless, the external disturbance must be considered to achieve the highly accuracy requirement. In the mission phase of the re-entry and image acquisition, the attitude is subject to stringent constraints to ensure alignment of the deployed sail with the velocity vector and to prevent high angular rates that may adversely affect the quality of image acquisition. Thus, the active controller $\boldsymbol{\tau}_c$ is designed to guarantee pointing accuracy.

Define the attitude error matrix as

$$\mathbf{C}_e = \mathbf{C}_d^T\mathbf{C} \tag{15}$$

And, the vector form of the attitude error can be formulated as

$$\mathbf{e}_R = \frac{1}{2}(\mathbf{C}_e - \mathbf{C}_e^T)^\vee \tag{16}$$

where $(\cdot)^\vee$ is the inverse of the skew-symmetric mapping, as known as the vee operator [10].

To design the attitude controller, the following assumptions are made:

Assumption 1. *There exist positive constants* β_{Lg}*,* β_d *such that* $\|\mathbf{L}_G\| < \beta_{Lg}$*,* $\|\boldsymbol{\tau}_d\| < \beta_d$*.*

The controller can be designed as

$$\boldsymbol{\tau}_c = -k_p\mathbf{e}_R - k_\omega\boldsymbol{\omega} + [\boldsymbol{\omega}]^\times\mathbf{J}\boldsymbol{\omega} \tag{17}$$

where k_p and k_ω is the control gain to be designed. Consider the Lyapunov function candidate

$$\mathbf{V} = \frac{1}{2}\boldsymbol{\omega}^{\mathrm{T}}\mathbf{J}\boldsymbol{\omega} + k_p\boldsymbol{\Psi}(\mathbf{C}_e) \tag{18}$$

where $\boldsymbol{\Psi}(\mathbf{C}_e)$ is the configuration error function

$$\begin{gathered}\boldsymbol{\Psi}(\mathbf{C}_e) = \frac{1}{2}\mathrm{tr}(\mathbf{I} - \mathbf{C}_e) \\ \dot{\boldsymbol{\Psi}}(\mathbf{C}_e) = \mathbf{e}_R^T\boldsymbol{\omega}\end{gathered} \tag{19}$$

Taking the time derivative of the Lyapunov function, it can be obtained that

$$\dot{\boldsymbol{V}} = \boldsymbol{\omega}^{\mathrm{T}}\mathbf{J}\dot{\boldsymbol{\omega}} + k_p\dot{\boldsymbol{\Psi}}(\mathbf{C}_e) \tag{20}$$

Substituting (2) and (17)into (20), it can be rewritten as

$$\begin{aligned}\dot{\boldsymbol{V}} &= \boldsymbol{\omega}^{\boldsymbol{T}}\left(-k_p\mathbf{e}_R - k_\omega\boldsymbol{\omega} + \mathbf{L}_G + \boldsymbol{\tau}_d\right) + k_p\mathbf{e}_R^T\boldsymbol{\omega} \\ &\leq \|\boldsymbol{\omega}\|\|\mathbf{L}_G\| + \|\boldsymbol{\omega}\|\|\boldsymbol{\tau}_d\| - k_\omega\|\boldsymbol{\omega}\|^2\end{aligned} \tag{21}$$

Therefore, it can be deduced that $\dot{V} < 0$ if

$$\|\boldsymbol{\omega}\| > \frac{\beta_{Lg} + \beta_d}{k_\omega} \tag{22}$$

It can be guaranteed that the norm of the angular velocity vector is bounded, and the tracking performance can be derived from the designed parameters of the controller. As the angular velocity vector $\boldsymbol{\omega}$ is bounded, and the time derivation term $\dot{\boldsymbol{\omega}}$ is also bounded. Hence, it is obvious that the error $\mathbf{e}_R$ remains bounded and converges to a neighborhood of zero. The boundary is determined by the control gain and the boundary of the external disturbance term. Consider the disturbance-free case at the equilibrium point

$$\dot{\boldsymbol{V}} = -k_\omega\|\boldsymbol{\omega}\|^2 \leq 0 \tag{23}$$

The largest invariant set is

$$\mathcal{M} = \left\{(\boldsymbol{\omega}, \mathbf{e}_R)\middle|\dot{\boldsymbol{V}} = \mathbf{0}\right\} = \{(\boldsymbol{\omega}, \mathbf{e}_R)|\boldsymbol{\omega} = \mathbf{0}\} \tag{24}$$

In the invariant set $\mathcal{M}$, the reduced dynamic equation can be obtained

$$\dot{\boldsymbol{\omega}} = -k_p\mathbf{J}^{-1}\mathbf{e}_R \tag{25}$$

This implies that unless the attitude error $\mathbf{e}_R$ is also zero, $\dot{\boldsymbol{\omega}} \neq \mathbf{0}$. In other words, the system's state cannot remain in $\mathcal{M}$ unless both $\boldsymbol{\omega} = \mathbf{0}$ and $\mathbf{e}_R = \mathbf{0}$. As a result, LaSalle's Invariance Principle guarantees that all trajectories of the closed-loop system converge asymptotically to this unique equilibrium point, which corresponds to the desired attitude and zero angular velocity.

Figure 10 and Figure 11 show the system response of the control system; the results demonstrate that the close loop control framework ensures effective stabilization of the system. And the control input is shown in Figure , it does not exceed the hardware limits.

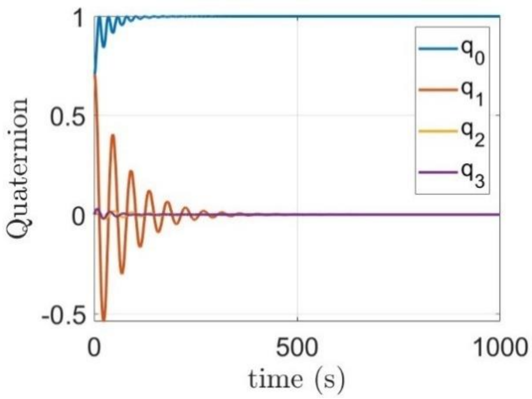

Figure 10 The system response of the attitude.

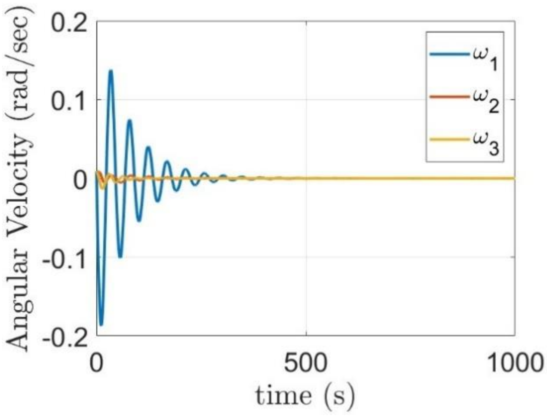

Figure 11 The system response of the angular velocity.

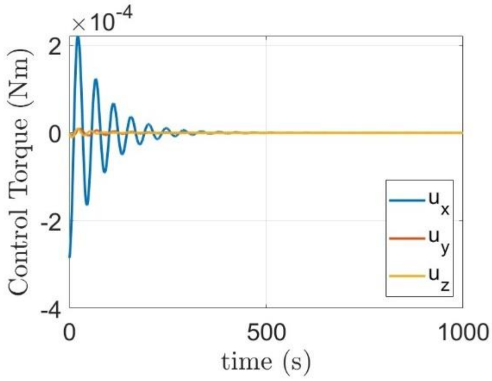

Figure 12 The control input.

The pointing accuracy of the satellite attitude tracking can be estimated by (22). And, As the system state converges toward the equilibrium configuration, the upper bound of the gravity gradient torque is expected to asymptotically approach zero. The design parameters can be adjusted according to on-orbit environmental disturbances, the maximum torque output of the hardware, and specific mission requirements.

This study introduces a deployment system to adjust the equilibrium attitude of a low earth orbit satellite. The gravity gradient torque approaches zero as the satellite's attitude converges to the equilibrium point. Thus, the attitude can be passively adjusted without the expenditure of additional energy. Under the presence of external disturbances and high pointing accuracy requirements, the feedback control system is activated to ensure the desired attitude is maintained. The feedback controller is designed to guarantee robust performance in the presence of exogenous disturbances. Furthermore, the asymptotic stability of the nonlinear dynamic system is provided in the sense of Lyapunov. Finally, the simulation results verify that the spacecraft can achieve the attitude tracking requirements in the presence of external perturbation, such as aerodynamic torque.

4. Orbital and aerodynamics analysis

4.1 Orbit Simulation

To analyze the orbital parameters, STK (Systems Tool Kit) software was used, with reference to the Falcon 9 Launch User's Manual (SpaceX, 2021). A sun-synchronous orbit was selected, featuring a semi-major axis of approximately 6910 km, a perigee of 523.3 km, an apogee of 537.7 km, and an inclination of 97.5°, resulting in an orbital period of 95.1 minutes. Also, one of the mission objectives is to deploy a sail to induce orbital decay, ultimately leading the CubeSat to re-enter Earth's atmosphere. STK's High-Precision Orbit Propagator (HPOP) was used to simulate the mission, predicting key parameters such as orbital lifetime and communication windows.

Atmospheric drag is the most critical factor influencing the satellite's orbital decay and lifetime. The drag force is affected not only by the drag coefficient but also by variations in atmospheric density, which is strongly influenced by solar activity. According to NASA forecasts, shown in Figure 13, solar activity is expected to peak in 2025, with solar flux reaching approximately 200 solar flux units (sfu). Higher solar flux increases atmospheric density, thereby accelerating orbital decay. After this peak, solar flux is projected to decrease steadily, reaching around 70 sfu by 2031. Therefore, shown in Figure 14, the analysis results show that the satellite's shortest predicted lifetime occurs in early 2025 due to maximum solar activity. The longest lifetime is expected between 2029 and 2030, with a gradual decline afterward as solar activity begins to rise again.

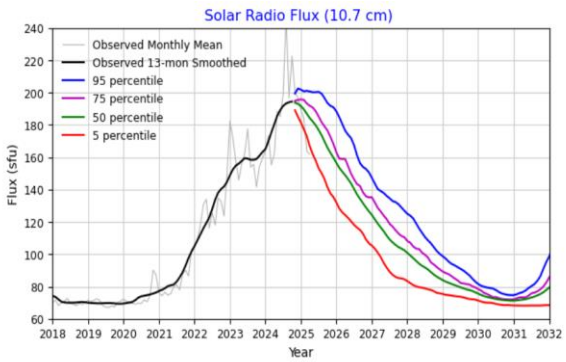

Figure 13 Forecasts of the solar radio flux from NASA.

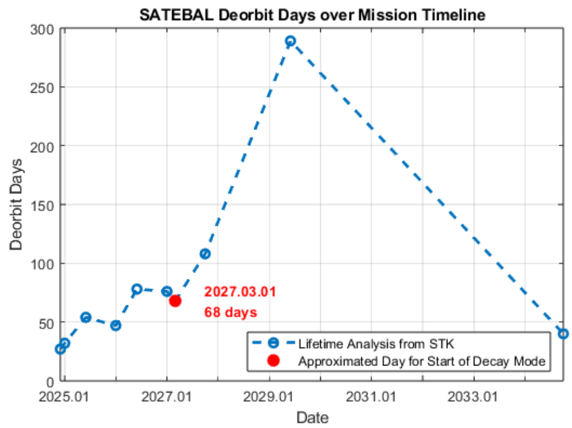

Figure 14 Lifetime estimation from STK.

Based on the analysis of deorbit time and the mission timeline of SATEBAL, shown in Figure 12, the CubeSat can begin its decay mode from March 2027 and re-enter the atmosphere 68 days after sail deployment. Once it descends to 200 km altitude, it will take about 2 additional hours to complete re-entry. This 68-day decay period marks the operational duration of the SATEBAL mission. During this phase, SATEBAL will deploy its drag sail, collect data, and maintain communication with the ground station, ensuring the mission's successful execution and completion.

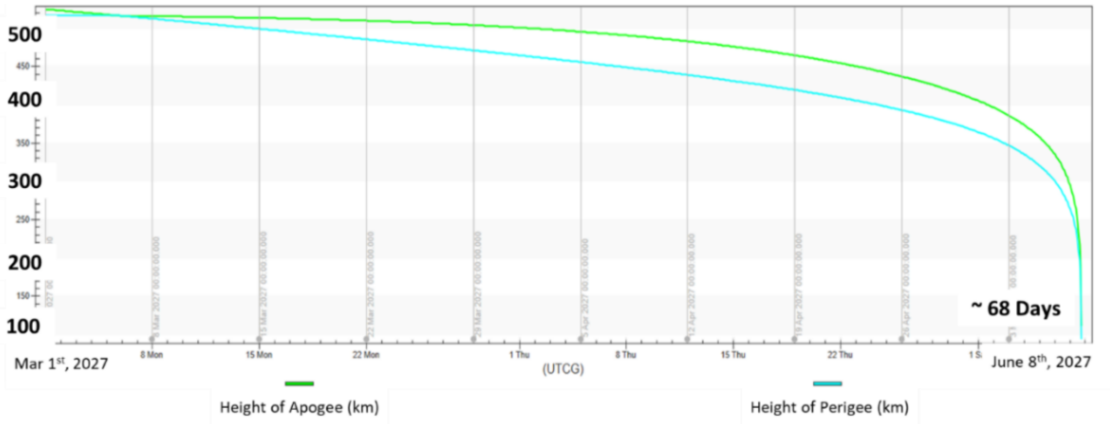

Figure 15 Orbital decay time and re-entry time estimation by STK.

4.2 Aerodynamic Force Analysis

In Low Earth Orbit (LEO), aerodynamic forces are significant due to residual atmospheric particles, especially for satellites with large surface areas or operating in Very Low Earth Orbit (VLEO). A low Knudsen number ($Kn=\lambda/L$) indicates a transitional flow regime between continuum and free molecular flow. These forces—shaped by satellite geometry and surface reflection properties—generate torques that affect attitude. Based on Walter (2008), satellites between 150 and 600 km altitude typically exhibit a drag coefficient of $C_D=2.2\pm0.2$.

This section analyzes a CubeSat with a deployed drag sail to examine how aerodynamic forces influence orbital decay and attitude stability. Drag coefficients are estimated. Two methods—Free Molecular Flow (FMF) (Vinh et al., 1980 and Wiesel, 1989) and Response Surface Methodology (RSM) (Mehta et al., 2014)—are used and cross-validated to ensure accurate drag modeling in the rarefied orbital environment.

4.2.1 Atmospheric Density Models

To model atmospheric density, the study compares several existing models. The NRLMSISE-00 model was selected for altitudes around 480–500 km, and the DTM (Drag Temperature Model) was used for lower altitudes (300–500 km). These were further supported by the Piecewise-Exponential Model, which provided a continuous curve of atmospheric density variation with altitude, improving the fidelity of drag coefficient estimation.

4.2.2 Free Molecular Flow Analysis

In the free molecular regime, aerodynamic forces are governed by the momentum exchange between individual gas molecules and the satellite surface. (Vinh et al., 1980 and Wiesel, 1989) The linear momentum transfer p is influenced by the incidence angle and the molecular scattering model. The basic momentum exchange equations are as follows:

$$p = \int F(\theta, \phi) dA \tag{26}$$

Where $F(\theta, \phi)$ is the force per unit area as a function of incidence and azimuth angles, and dA is the surface element.

Two primary reflection models are considered:

- **Specular reflection**, where molecules reflect with preserved angle symmetry,
- **Diffuse reflection**, where molecules are re-emitted in random directions.

The drag coefficient for each reflection type is computed differently. For instance, assuming a flat surface and cube geometry, the drag coefficient under specular and diffuse reflection can be expressed as:

- **Specular:**

$$C_{D,spec} = \frac{2}{\pi} \cos^2 \theta \tag{27}$$

- **Diffuse:**

$$C_{D,diff} = 2 \cos \theta \tag{28}$$

Where θ is the incidence angle. The total drag is then the integration over all possible surface orientations, weighted by their surface area and orientation angles.

Assuming the CubeSat rotates symmetrically along a body-fixed axis, a spherical coordinate system (θ,ϕ) is used to describe surface orientation. The drag coefficient as a function of angle of attack was computed, and results showed that for tumbling CubeSats, the average drag coefficient fluctuated but centered around $C_D \approx 2.4 \pm 0.2$, aligning well with empirical estimates from prior literature.

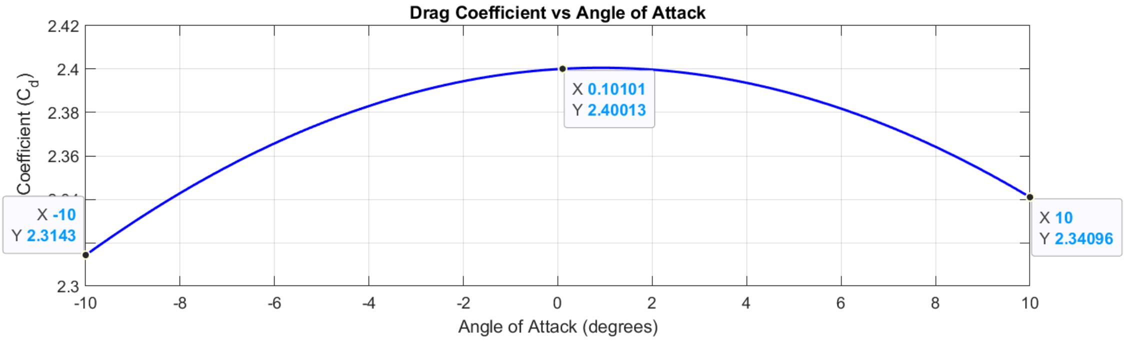

Figure 16 Drag coefficients result at different angles of attack of the CubeSat under the FMF method.

4.2.3 Response Surface Methodology (RSM)

To improve computational efficiency and accommodate CubeSat's complex geometry, RSM (Mehta et al., 2014) is applied to model drag coefficients using surrogate models derived from Test Particle Monte Carlo (TPMC) simulations.

The process begins with Latin Hypercube Sampling (LHS) to generate a diverse 1000-point parameter space. Each point is a configuration of environmental and geometric parameters (e.g., satellite velocity, surface temperature, atmospheric composition). The drag coefficients derived from TPMC simulations are then fitted using a Gaussian Process Regression model.

Validation on a spherical object yielded a root-mean-square percentage error below 0.3%. When applied to complex geometries like the GRACE satellite, Hubble Space Telescope (HST), and the ISS, drag coefficient errors are contained within 1%, demonstrating high accuracy.

Subsequent steps include:

1. **Projection Area Modeling:** Using the RSM_Area module, the projected area of the satellite is computed for different pitch ϕ and yaw θ angles.
2. **Ballistic Coefficient Computation:** The projected area data feeds into drag and ballistic coefficient calculations.
3. **RSM_Cd Module:** Combines environmental and geometric data to predict C_D under varying flight conditions.

For the deployed drag sail (1 m × 1 m per side), the RSM model computed drag coefficients as functions of pitch angle. The results are shown in Figure 17-19 and $C_D \approx 2.31 \pm 0.05$ at different elevation angles. These results are consistent with FMF-based calculations, offering further confidence in the model's predictive power.

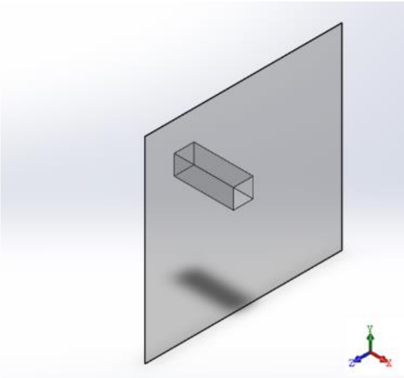

Figure 17 Simplified model inside the RSM method

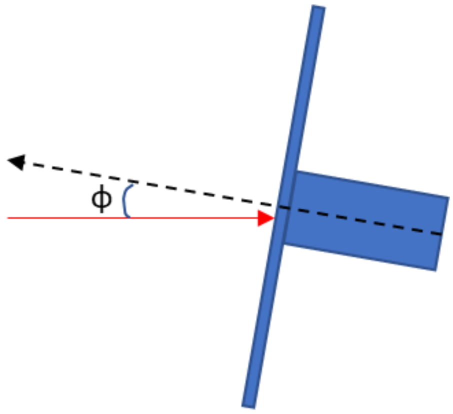

Figure 18 Relationship between the model and the elevation angle

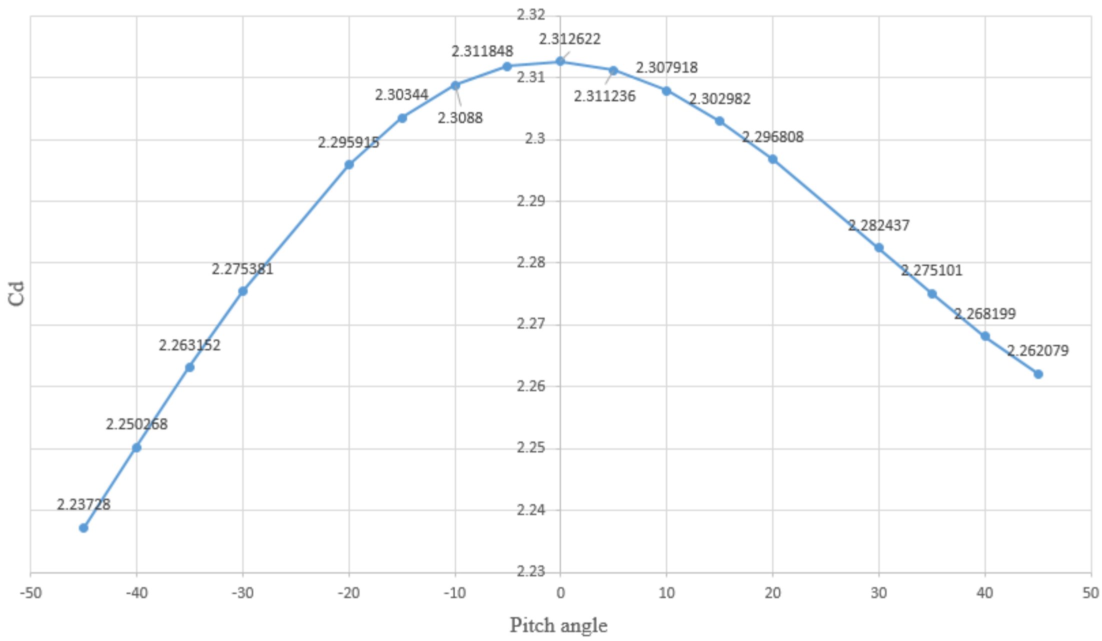

Figure 19 Drag coefficients result at different angles of attack of the CubeSat under the RSM method.

4.3 Summary of orbital and aerodynamic analysis

The analysis confirms that deploying a drag sail drastically reduces CubeSat orbital lifetime, as verified by STK simulations and consistent with existing literature. To support precise deorbit predictions and attitude control during this critical phase, the study applied both Free Molecular Flow theory and Response Surface Methodology to estimate aerodynamic drag coefficients under varying conditions.

Results from both methods showed close agreement, particularly in the -5° to 5° pitch angle range, where $C_D \approx 2.2$, validating the methodology against Walter (2008). Although these results are a preliminary result of aerodynamic analysis, it provides the feasibility of the decay-mode mission. As the decay mode begins, the GNSS and attitude data can provide the validation of the mission.

5. Space segment description and analysis

5.1 Structural and Mechanisms Subsystem (SMS) and Mass Budget

SMS is primarily responsible for the overall satellite structure design, spatial arrangement, and strength analysis. Based on the CubeSat101 document published by NASA (2017), SATBAL's subsystems are arranged within the satellite according to their specific requirements. In this CubeSat, the X-axis aligns with the flight direction, while the Z-axis faces the Earth. The mass budget is estimated based on the specifications and materials of each subsystem. The aim is to keep the total weight under 6 kilograms in accordance with the limits specified for a 3U CubeSat in the CubeSat 101 document.

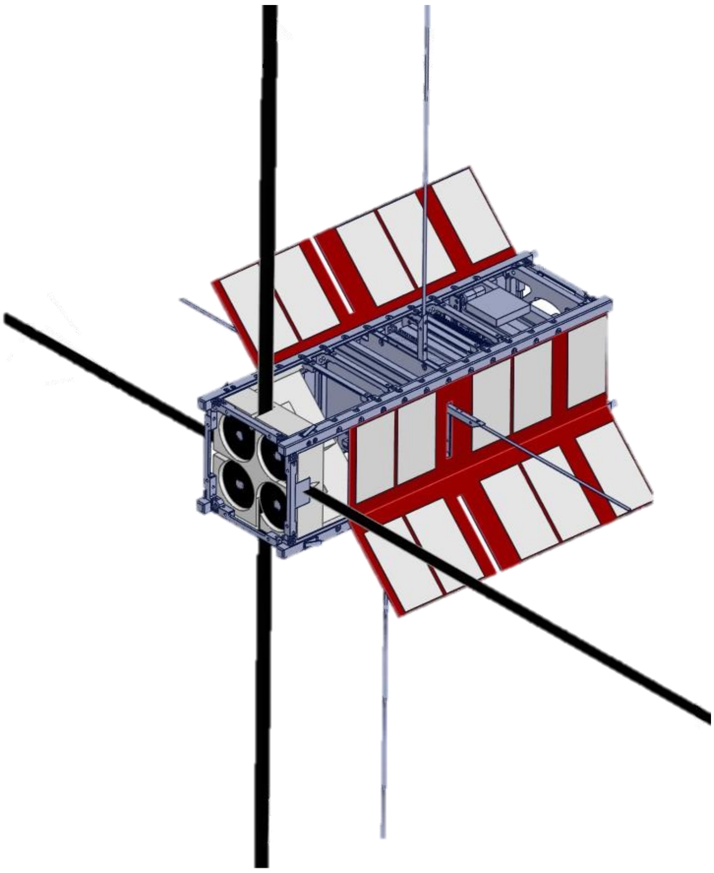

Figure 20 3U Structural and Mechanism Subsystem

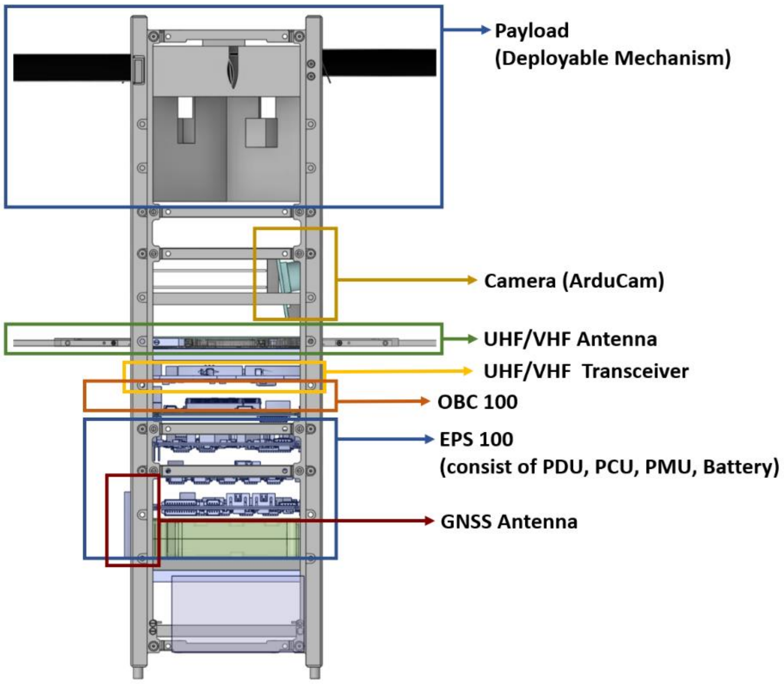

Figure 21 Subsystem allocation in SATBAL

Part	Mass (g)	Mass with margin (g)	Percent of total mass (%)
Liscotech OBC100	55	60.5	3%
Liscotech EPS100 Module	568	624.8	27%
ISISPACE VHF uplink/UHF downlink Full Duplex Transceiver	175	192.5	8%
ISISPACE CubeSat Antenna System for 1U/3U	100	110	5%
Solar cell+ Solar panel	200	220	10%
Structure	500	600	24%
ArduCAM	20	22	1%
Deployment Mechanism	200	220	10%
GNSS Antenna	264	290	13%
Total mass	2082	2339.8	100%

Figure 22 Mass budget

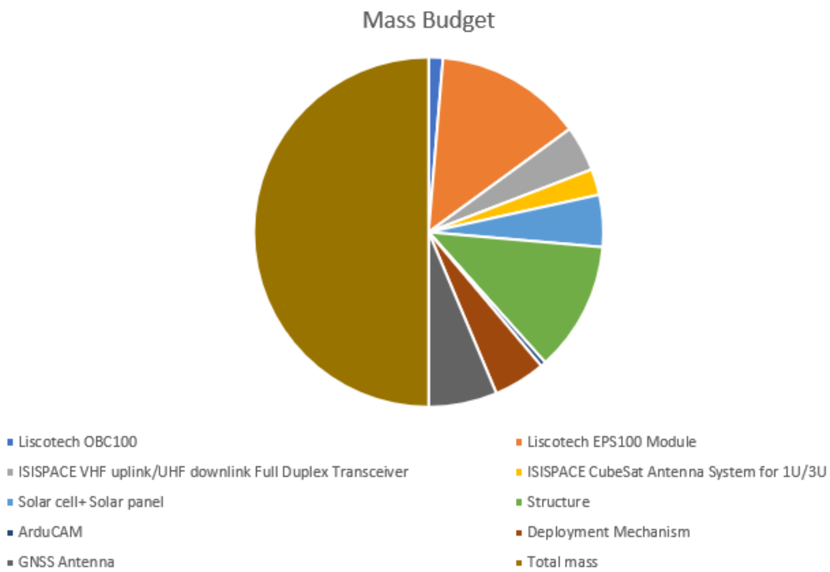

Figure 23 Percent of total mass

5.2 Camera-ArduCAM

ArduCAM is installed to capture images of the deployed sail, as well as in-flight images during the mission. To ensure full coverage of the sail's quarter view, the camera is mounted at an optimal angle of 81°, paired with a 120° wide-angle lens to capture the entire process. The ArduCAM integrates an image processing chip, reducing the computational load on the flight computer. Controlled via I2C, it allows real-time adjustments to image resolution and exposure time, offering flexibility to adapt to varying conditions in space, such as communication delays or environmental changes. The camera captures images in JPG format at a resolution of 1024x768 pixels, which can be downlinked to the ground station, providing visual proof of the sail's successful deployment. This system is critical for ensuring mission success while offering flexibility in capturing additional imagery based on evolving mission needs.

5.3 On-Board Data Handling (OBDH) Subsystem

In this satellite mission, the On-Board Data Handling (OBDH) system plays a pivotal role not only in orchestrating inter-subsystem communication and data storage but also in executing the semi-passive attitude stabilization strategy, which utilizes a controllable center of mass offset mechanism. This alternative approach replaces the conventional aerodynamic drag sail and relies on the satellite's internal mass displacement to generate passive torque for attitude control.

The OBDH system is based on the OBC100 flight computer developed by Liscotech System Co., Ltd., utilizing the TMS570LC4357 microcontroller, a dual-core lockstep processor designed for fault tolerance in radiation-prone space environments. The system supports UART, I2C, SPI, and GPIO communication protocols, and is equipped with hardware ECC on RAM and Flash, watchdog timers, and low-power modes. This robust hardware foundation supports the real-time responsiveness and reliability required for autonomous satellite operations in Low Earth Orbit.

Figure 24 CubeSat On-board Computer which is used

The software architecture is built upon FreeRTOS, a lightweight real-time operating system that facilitates deterministic task scheduling and inter-task communication. This foundation allows the OBDH to maintain reliable, concurrent control over time-critical satellite operations. The architecture is composed of multiple layers. The hardware abstraction layer manages the physical interface to sensors and subsystems via I2C, SPI, UART, ADC, and GPIO. Above this, middleware services handle functionalities such as time management, data logging, cyclic redundancy checking, and file system access. The application layer orchestrates system-level tasks such as camera triggering, power state management, and telemetry packaging.

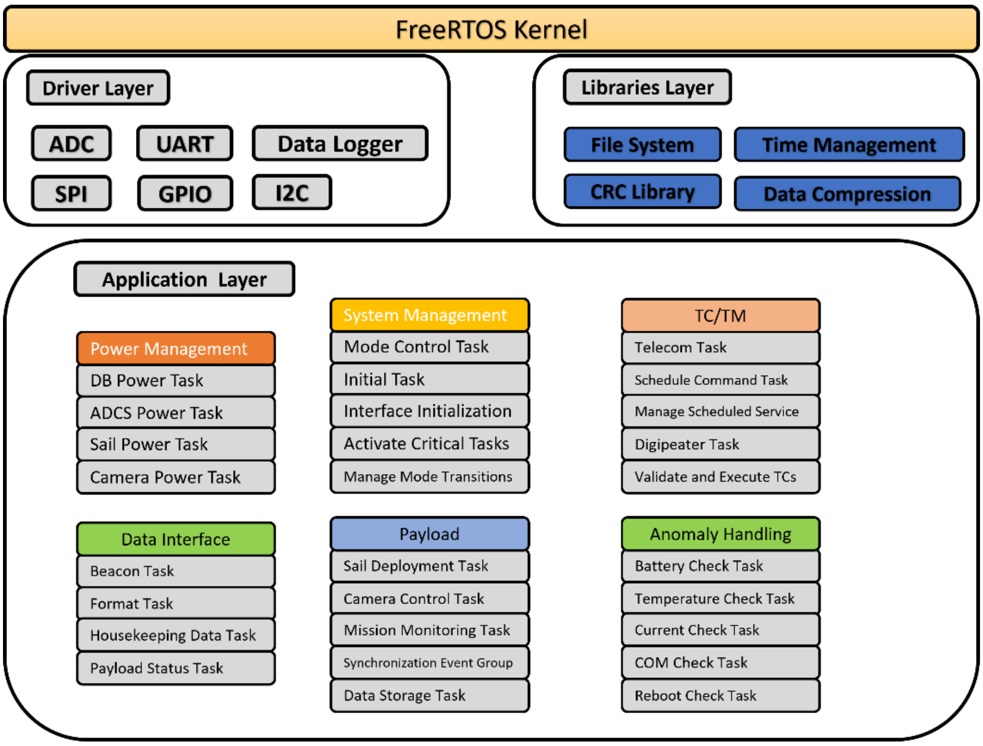

Figure 25 The software architecture built upon FreeRTOS

Upon deployment, the OBDH initiates a countdown sequence during which it verifies antenna deployment, initializes mission parameters, and activates baseline tasks. This is followed by the detumbling process via the ADCS subsystem and the gradual activation of other mission-critical modules such as the camera and decay mechanism. Throughout the mission lifecycle, FreeRTOS tasks transition across six defined operational states: Deployment, Initial Stabilization, Nominal Operation, Decay, Safe Mode, and Recovery. These transitions are governed by a finite-state machine model encoded within the OBDH logic, with each phase activating or deactivating specific tasks depending on power availability and mission needs.

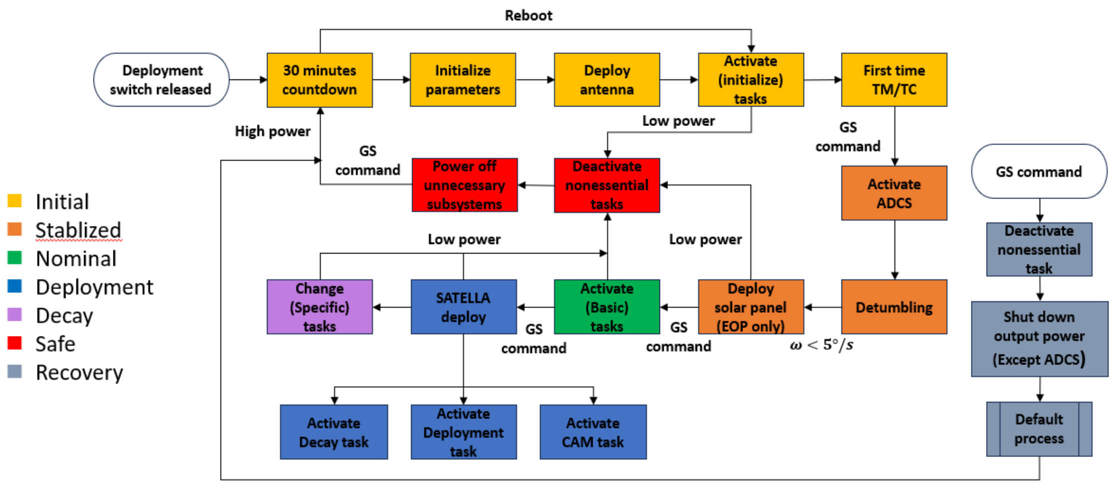

Figure 26 operational states of FreeRTOS tasks transition.

A distinctive feature of this mission is the implementation of a semi-passive attitude stabilization mechanism. Rather than relying on an external drag sail, the satellite adjusts its center of mass through a movable mass controlled by the OBDH. This mechanism uses a linear actuator to reposition a calibrated mass along a fixed axis, inducing passive restoring torque to stabilize the satellite. The actuator is commanded based on real-time quaternion data from the ADCS or on predefined sequences. FreeRTOS tasks ensure closed-loop control by continuously monitoring the actuator position, timing windows, and thermal conditions to guarantee safe execution.

Data management is a critical function of the OBDH system. Sensor and status data are first buffered in RAM and subsequently written to onboard Flash memory at fixed intervals. Every five minutes, these data blocks are synchronized and archived into a Micro SD card for long-term retention. The storage architecture is designed with multiple levels of protection: all data packets are appended with CRC-32 checksums for error detection, flash memory is managed with a wear-leveling algorithm and bad-block avoidance strategy, and capacitor-based power failure protection ensures write completion during voltage drops. To avoid data corruption from concurrent write operations, FreeRTOS mutexes and semaphores are used to serialize access to shared memory and file systems.

During nominal operations, the OBDH manages beacon broadcasting at fixed intervals over VHF/UHF bands. Each beacon packet contains the satellite ID, GNSS lock status, battery voltage, movable mass offset, and ADCS status. These data are not only transmitted to the ground station but also logged in non-volatile storage. The telecommand interface allows ground operators to send uplinked instructions to control movable mass position, toggle beacon functions, or request system diagnostics. Each incoming command undergoes CRC validation and timestamp verification before execution. Successful execution is acknowledged during the next telemetry downlink session.

To ensure resilience, fault detection and recovery mechanisms are integrated throughout the software. Each major FreeRTOS task maintains a heartbeat signal, monitored by the hardware watchdog; failure to respond triggers a localized reset. Critical events such as movable mass actuator timeouts, power surges, or sensor anomalies are detected and logged, along with diagnostic codes and timestamps. In case of persistent failure, the OBDH transitions the system into Safe Mode, shutting down nonessential subsystems and awaiting ground intervention.

In summary, this satellite's OBDH system exemplifies a tightly integrated, real-time software framework that supports autonomous satellite operation under constrained resources. Through its FreeRTOS-based design, structured task management, and robust data protection mechanisms, the OBDH not only ensures baseline functionality but also enables the experimental center-of-mass-based attitude stabilization, forming a platform for future satellite innovations.

5.4 Electrical Power Subsystem (EPS) and Power Budget

The Electrical Power Subsystem (EPS) harvests solar energy and stores it in batteries. It then distributes regulated voltages to all spacecraft subsystems throughout every mission phase. It must operate reliably from launch, through dormancy, to nominal science operations.

5.4.1 Design Requirements of EPS

(1) All-Mode Output

The CubeSat shall provide sufficient power at the appropriate voltage, either by solar array generation or battery, to meet the power requirements of all satellite subsystems in all modes of operation.

Table 2 The technical specifications.

Power Budget of SATELLA			[W/per Orbit] (95min.)										
Subsystems	Components	Power Consumption(W)	Initial Detumbling	Initial Stabilizing	Safe	Nominal	Phase1 Imaging	Phase 1 Downlink	Sail Deployment	Decay Nominal	Phase 2 Imaging	Phase 2 Downlink	Supply Voltage(V)
OBC	OBC100	1.5	1.5	1.5	1.5	1.5	1.5	1.5	1.5	1.5	1.5	1.5	5V
EPS	EPS100	1.1	1.1	1.1	1.1	1.1	1.1	1.1	1.1	1.1	1.1	1.1	
ADCS	ADCS-10m(MCB+CMG-10m)	1	1	1	0	1	1	1	1	1	1	1	3.3V/5V
TT&C	U/V Band Transceiver (RX)	0.48	0.48	0.48	0.48	0.48	0.48	0.48	0.48	0.48	0.48	0.48	6.5 – 20 V DC
	U/V Band Transceiver (Beacon)	0.0288	0.0288	0.0288	0.0288	0.0288	0.0288	0.0288	0.0288	0.0288	0.0288	0.0288	
	U/V Band Transceiver (TX)	4	0	0	0	0.42	0	0.42	0	0.00	0	0.42	3.3V/5V
	Antenna(Nominal)	0.04	0.04	0.04	0.04	0.04	0.04	0.04	0.04	0.04	0.04	0.04	3.3V DC +/-10%
GPS	Orion B16-C1	0.58	0.58	0.58	0	0.58	0.58	0.58	0.58	0.58	0.58	0.58	5V
Payload	Arducam OV5642	1.95	0	0	0	0	0.20475	0	0	0	0.20475	0	3.3V/5V
	Motor-Sail	5	0	0	0	0	0	0	0.526 (10 min)	0	0	0	12V
	Motor-Gravity Gradient Boom	9.6	0	0	0	0	0	0	1.011 (10 min)	1.011 (10 min)	0	0	
Power Consumption(W/per Orbit)			4.73	4.73	3.15	5.15	4.93	5.15	6.27	5.74	4.93	5.15	
Reserved 15% for Converter Efficiency(W/per Orbit)			0.71	0.71	0.47	0.77	0.74	0.77	0.94	0.86	0.74	0.77	
Total Average Power Consumption(W/per Orbit)			5.44	5.44	3.62	5.92	5.67	5.92	7.21	6.60	5.67	5.92	
Power Generation(W/per Orbit)		Stowed	5.50	5.50	5.50	-	-	-	-	-	-	-	
		Deployed			9.06	9.06	9.06	9.06	9.06	9.06	9.06	9.06	
Reserved 10% for PV Converter Efficiency(W/per Orbit)		Stowed	0.55	0.55	0.55	-	-	-	-	-	-	-	
		Deployed			0.91	0.91	0.91	0.91	0.91	0.91	0.91	0.91	
Total Average Power Generation(W/per Orbit)		Stowed	4.95	4.95	4.95	-	-	-	-	-	-	-	
		Deployed			8.15	8.15	8.15	8.15	8.15	8.15	8.15	8.15	
Power Margin(%)		Stowed	-9.86	-9.86	26.85	-	-	-	-	-	-	-	
		Deployed			55.59	27.38	30.42	27.38	11.63	19.06	30.42	27.38	

(2) Long-Dormancy Restart

The CubeSat shall be able to be commissioned in orbit following the last powered-down state without battery charging, inspection or functional testing for a period of up to 8 months.

(3) Launch-Hold-Off

The CubeSat shall be powered OFF during the entire launch and until it is deployed from the P-POD after 30 seconds.

(4) Battery Depth-of-Discharge Limit

The maximum allowable depth-of-discharge (DoD) of the battery shall not exceed 35%. Depth of Discharge(DoD) calculation :

$$\text{DoD} = \frac{\text{Energy Discharged}}{\text{Battery Capacity}} \times 100\% \quad (29)$$

5.4.2 Hardware Components

(1) MPPT Module

The heart of the power system is the Liscotech EPS100, which implements a high-efficiency Maximum Power Point Tracking (MPPT) algorithm, includes integrated heaters for cold-temperature startup, and uses FRAM (Ferroelectric Random Access Memory) to retain critical data across power cycles. It is optimized for 3U/6U CubeSat form factors and includes resettable fuses and a deployment-switch interface.

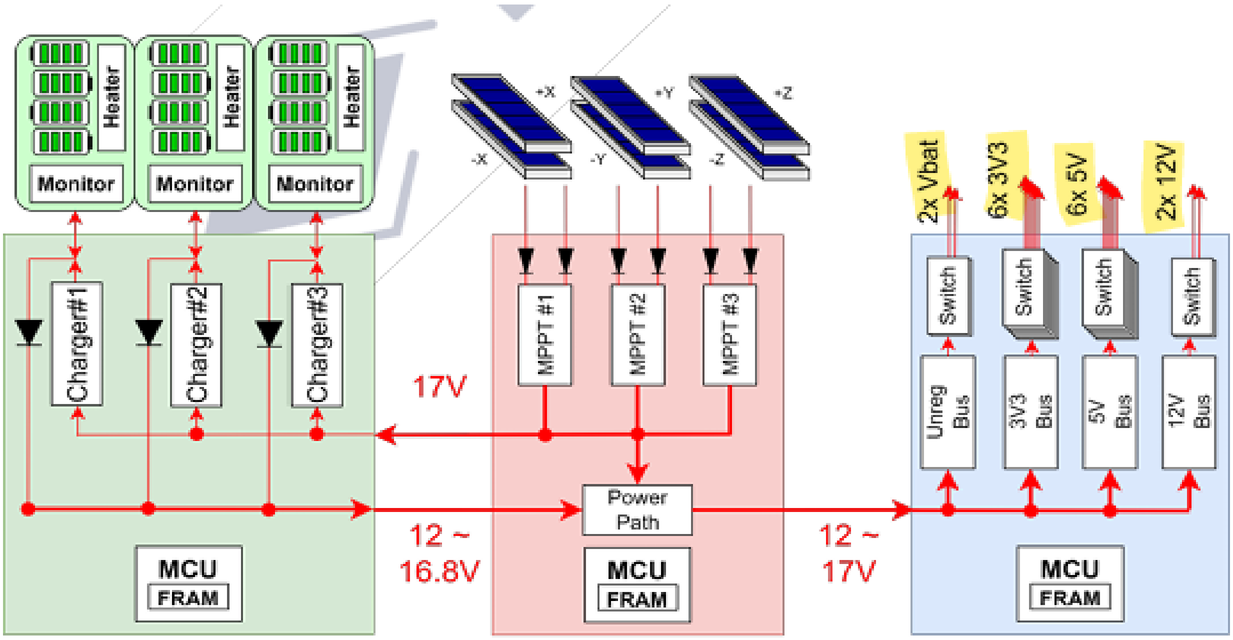

Figure 27 EPS100 Block Diagram

(2) Solar Cell Type

Power is generated by LiveStrong/Spectrolab CIC XTE-SF triple-junction GaAs panels—qualified to the AIAA-S111 standard, rated at 32.2 percent BOL efficiency (27.9 percent EOL), and tested to withstand 1 MeV electron fluence with accompanying EL imagery and I–V curves.

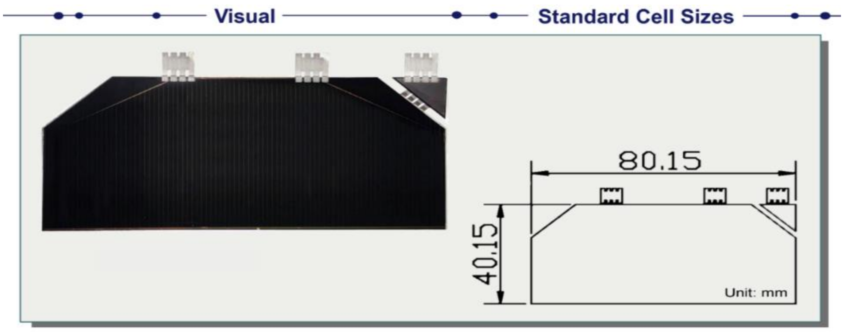

Figure 28 The size of solar cell

(3) Battery Pack

Energy is stored in a 45 Wh Li-ion pack arranged as 4S1P × 3 and 3S1P × 2.

5.4.3 EPS Block Diagram

As shown in Fig. the EPS comprises solar arrays feeding a PCU with MPPT, a BMU-managed 4S1P Li-ion battery pack, and a PDU that supplies regulated 3.3 V, 5 V, 12 V and raw battery rails to all subsystems ensuring seamless power from launch through dormancy to science operations.

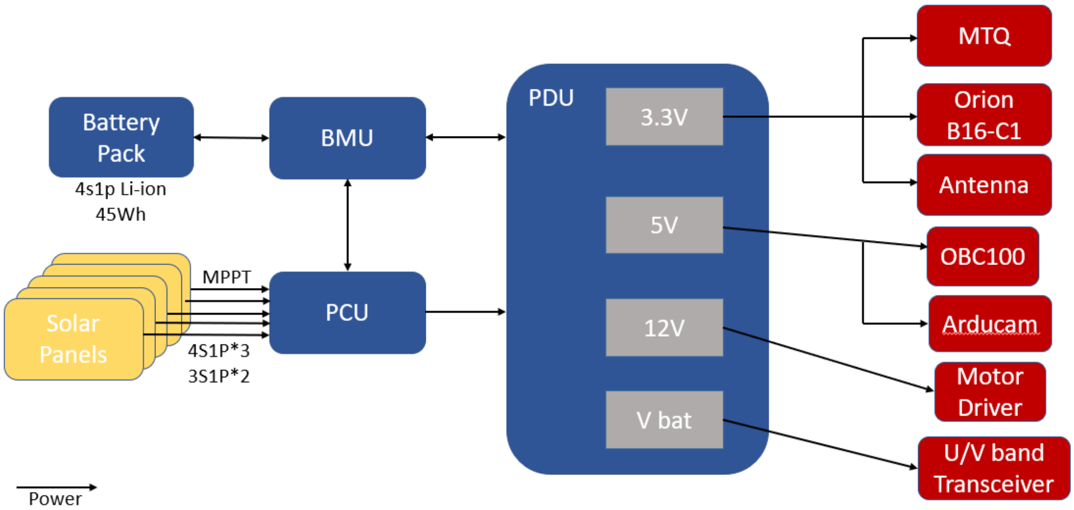

Figure 29 The architecture diagram of EPS and other subsystems.

5.4.4 Solar Panel Configuration

This section describes the mechanical layout and deployment method of the EPS solar array. The array comprises five deployable panels: three configured as 4S1P (four cells in series, one string in parallel) and two as 3S1P. During launch, these panels are folded flush against the spacecraft's sides; once in the target orbit, hinge mechanisms swing them outward to maximize solar-capture area and ensure sufficient illumination in all attitudes.

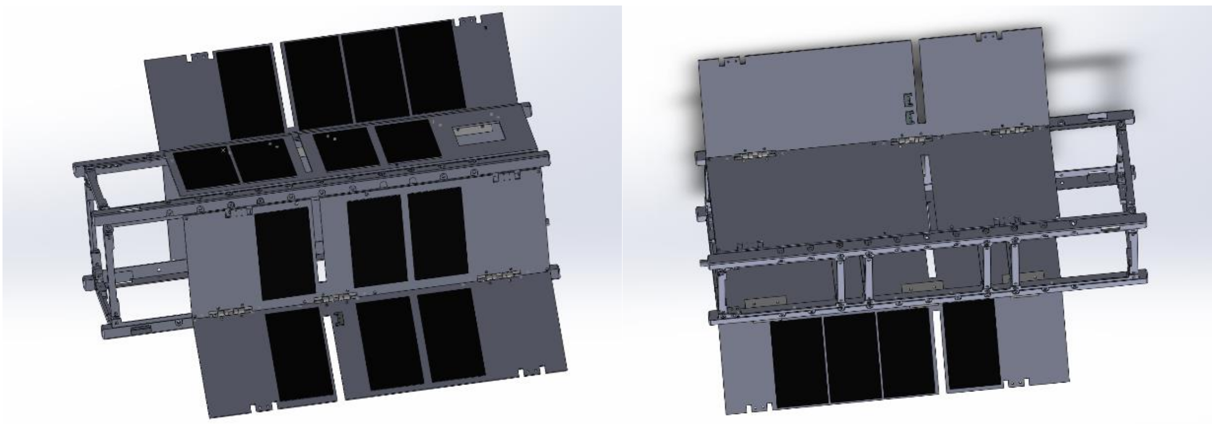

Figure 30 Solar panel deployed schematic diagram

5.5 Telemetry, Tracking, and Command (TT&C) Subsystem, Link Budget and ground station

SATEBAL employs a full-duplex VHF/UHF communication system developed by ISISpace, featuring a dipole antenna and a communication board known as TRXVU. The satellite uses UHF with Frequency Shift Keying (FSK) modulation for uplink and VHF with Binary Phase Shift Keying (BPSK) modulation for downlink. According to detailed link budget analysis, shown in Figure 1 of the report, the system achieves a robust link margin of 15.5 dB for uplink and 13.4 dB for downlink under approximate communication conditions. These margins exceed the required thresholds, demonstrating that the TT&C system is capable of maintaining stable communication in environments.

Uplink Command Budget:

Parameter:	Value:	Units:
Ground Station:		
Ground Station Transmitter Power Output:	20.0	watts
In dBW:	13.0	dBW
In dBm:	43.0	dBm
Ground Stn. Total Transmission Line Losses:	1.4	dB
Antenna Gain:	50.0	dBi
Ground Station EIRP:	61.6	dBW
Uplink Path:		
Ground Station Antenna Pointing Loss:	36.4	dB
Gnd-to-S/C Antenna Polarization Losses:	0.0	dB
Path Loss:	142.6	dB
Atmospheric Losses:	1.1	dB
Ionospheric Losses:	0.5	dB
Rain Losses:	0.0	dB
Isotropic Signal Level at Spacecraft:	-119.0	dBW
Spacecraft (Eb/No Method):		
------- Eb/No Method -------		
Spacecraft Antenna Pointing Loss:	0.0	dB
Spacecraft Antenna Gain:	0.0	dBi
Spacecraft Total Transmission Line Losses:	4.8	dB
Spacecraft Effective Noise Temperature:	337	K
Spacecraft Figure of Merrit (G/T):	-30.1	dB/K
S/C Signal-to-Noise Power Density (S/No):	79.5	dBHz
System Desired Data Rate:	9600	bps
In dBHz:	39.8	dBHz
Command System Eb/No:	39.7	dB
Demodulation Method Seleted:	AFSK/FM	
Forward Error Correction Coding Used:	None	
System Allowed or Specified Bit-Error-Rate:	1.0E-05	
Demodulator Implementation Loss:	1.0	dB
Telemetry System Required Eb/No:	23.2	dB
Eb/No Threshold:	24.2	dB
System Link Margin:	15.5	dB

Downlink Telemetry Budget:

Parameter:	Value:	Units:
Spacecraft:		
Spacecraft Transmitter Power Output:	4.0	watts
In dBW:	6.0	dBW
In dBm:	36.0	dBm
Spacecraft Total Transmission Line Losses:	1.0	dB
Spacecraft Antenna Gain:	0.0	dBi
Spacecraft EIRP:	5.0	dBW
Downlink Path:		
Spacecraft Antenna Pointing Loss:	0.0	dB
S/C-to-Ground Antenna Polarization Loss:	2.7	dB
Path Loss:	151.2	dB
Atmospheric Loss:	1.1	dB
Ionospheric Loss:	0.5	dB
Rain Loss:	0.0	dB
Isotropic Signal Level at Ground Station:	-150.5	dBW
Ground Station (EbNo Method):		
------- Eb/No Method -------		
Ground Station Antenna Pointing Loss:	0.0	dB
Ground Station Antenna Gain:	16.0	dBi
Ground Station Total Transmission Line Losses:	4.8	dB
Ground Station Effective Noise Temperature:	286	K
Ground Station Figure of Merrit (G/T):	-13.4	dB/K
G.S. Signal-to-Noise Power Density (S/No):	64.7	dBHz
System Desired Data Rate:	9600	bps
In dBHz:	39.8	dBHz
Telemetry System Eb/No for the Downlink:	24.9	dB
Demodulation Method Seleted:	BPSK	
Forward Error Correction Coding Used:	None	
System Allowed or Specified Bit-Error-Rate:	1.0E-06	
Demodulator Implementation Loss:	1	dB
Telemetry System Required Eb/No:	10.5	dB
Eb/No Threshold:	11.5	dB
System Link Margin:	13.4	dB

Figure 31 Link budget of uplink(left) and downlink(right)

5.5.1 Data downlink estimation

Based on preliminary orbit and link analysis from STK, the satellite is expected to maintain contact with the ground station for roughly 500 seconds per day during the early phase of the orbital decay. This estimate is based on a communication range of up to 2000 km and an elevation angle of around -23°. At the nominal rate of 9600 bps, which is the maximum capacity of the onboard transceiver, this equates to a theoretical maximum of 600 KB of data transmitted daily. Nonetheless, due to the anticipated disruptions, the actual daily transmission volume is expected to be significantly lower.

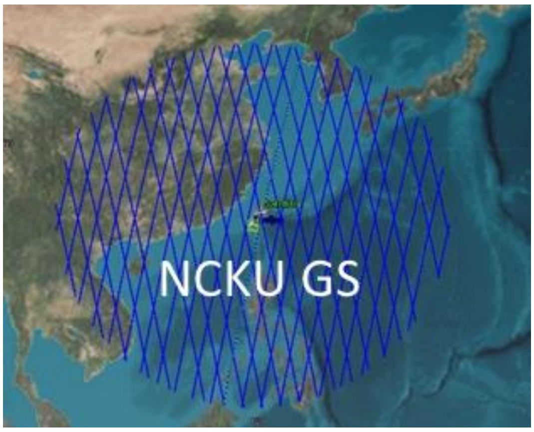

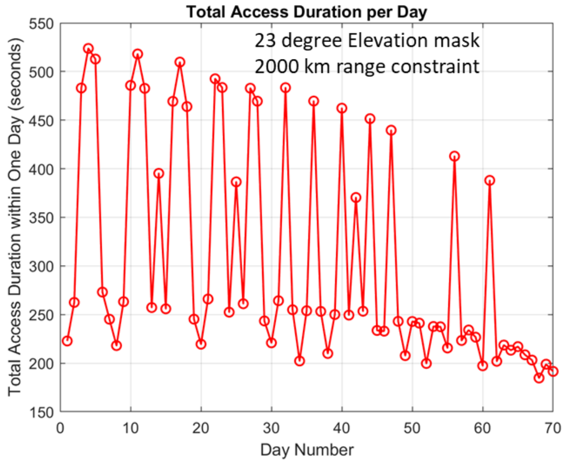

Figure 32 Communication distance of 2000 km away from the ground station(left) and the total access duration per day with 23-degree elevation mask(right) from the STK analysis.

To operate within this bandwidth-limited environment, SATEBAL employs a data prioritization and batching strategy, focusing on two primary data types:

- Image files captured by the ArduCAM system (.jpg, 1024×768 resolution), approximately 330 KB each.
- GNSS data in NMEA format (Position, Velocity, and Time only), totaling about 446.4 KB per orbit (every 90 minutes).

According to the STK analysis, the mission report is:

- Transmitting a single image requires around 402 seconds.
- Sending a full GNSS dataset takes approximately 544 seconds.

Both durations nearly exhaust or exceed the estimated daily downlink window, making it essential to optimize transmission efficiency.

5.5.2 Mission transmission strategy

To manage this constraint, the TT&C subsystem operations are split into two phases:

(1) Before Sail Deployment:

Data is transmitted on alternating days—images on one day, GNSS data the next. If an image cannot be completely transmitted in one pass, subsequent passes prioritize finishing the same image before switching to GNSS data. This prevents loss of partial files and ensures that no transmission effort is wasted.

(2) After Sail Deployment:

As the satellite descends more rapidly, communication windows shorten. The transmission priority shifts to sending one complete image first, followed by as much GNSS data as possible. This cycle repeats until atmospheric reentry terminates the mission.

Ultimately, the success of this strategy relies heavily on the performance and responsiveness of the ground station infrastructure, including its ability to handle fragmented data sessions and maintain reliable links under limited-time constraints.

5.5.3 Ground station operation

To transmit and receive commands and data from SATEBAL, the ground station at DAA, NCKU is used. This ground station is designed to use a Yagi antenna with tracking capability to maintain alignment with the CubeSat throughout each pass. To support signal reception and decoding, a software-defined radio (SDR) system will be employed. This allows for flexibility in modulation schemes and supports real-time adjustments to match signal variations caused by Doppler shifts and atmospheric conditions. To organize the components and signal flow of the ground station, there are three processes:

(1) SDR process

SDR (Software Design Radio) is used to receive and process signals at the ground station. The software that is used in SDR is SDR Console or GNU Radio. These software are open-source software-defined radio platforms that include various signal processing modules. In this setup, the SDR receives analog RF signals from the antenna and converts them into digital baseband signals. These digitized signals are then transferred to the host computer and processed in software for tasks such as demodulation, decoding, and telemetry extraction.

(2) Antenna Control

All the antennas are connected to the rotator controller, which adjusts their azimuth and elevation angles to track the satellite. The rotator communicates with the GS computer through the Controller and PC interface. The GS computer will run PSTRotator, a software that calculates antenna pointing angles based on satellite orbital parameters and sends control signals to the rotator.

(3) Mission Operation Software

A mission operation software is designed to serve as an integrated user interface that combines various open-source tools into a single platform. It displays satellite position, health data, communication status, mission control and monitoring, etc. The data will be presented in a clear and structured format, enabling effective satellite monitoring and command transmission.

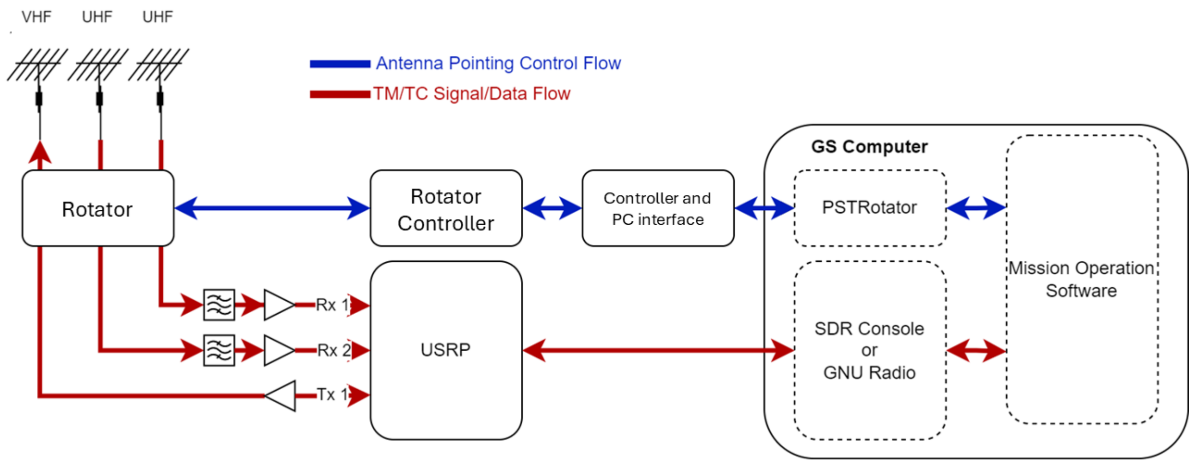

Figure 33 Organization of the Ground Station

5.5.4 Summary of TT&C subsystem

In anticipation of increased orbital decay and potential data loss, the mission team plans to share transmission responsibilities across multiple cooperative ground stations. This redundancy helps prevent data gaps caused by missed passes or local weather interference. Additionally, during the decay phase, the onboard computer (OBC) ensures that data packets are formatted and transmitted in a sequence optimized for completeness and redundancy, improving the odds that all critical mission data are successfully received before re-entry.

In conclusion, the SATEBAL TT&C subsystem is carefully designed to balance the mission's technical constraints with its scientific goals. Through a robust link budget, intelligent data management strategy, and ground station coordination, the system ensures reliable communication throughout the mission lifecycle. While the communication window is narrow and data volume limited, the structured approach to prioritization and redundancy helps maximize the scientific return of the mission.

5.6 Thermal Control Subsystem (TCS)

The thermal control system (TCS) is aiming at analyzing the temperature changes under different altitudes and making corresponding temperature control actions on the hottest and the coldest component of the CubeSat. Passive thermal control is chosen in this case to guarantee the electronic components of the satellite are in the required temperature margin. In this mission, there are two phases, so two phases temperature distribution of the satellite will be simulated.

5.6.1 Design Requirements of TCS

5.6.1.1 Design Requirements

The purpose of TCS is to maintain the temperature of the components in the range of their operating temperature range. For safety reasons, a temperature margin of 5 to 10 degrees Celsius is restricted in the simulation. The operating temperature range and the margin of the electronic components are listed in Table 3 below.

Table 3 Operating temperature range and safety margin for electronic components of each subsystem.

5~10°C Temperature margin

Subsystem	Component	Spec temp		Calculated temp	
		Min	Max	Min	Max
OBDH	OBC100	-25°C	65°C	-17°C	57°C
EPS	EPS100 Module	-25°C	65°C	-17°C	57°C
	Battery				
ADCS	ADCS-CMG-10m	-25°C	70°C	-17°C	62°C
TT&C	VHF uplink/UHF downlink Full Duplex Transceiver	-20°C	60°C	-12°C	52°C
	CubeSat Antenna System for 1U/3U	-20°C	60°C	-12°C	52°C
Payload 1	Solar Sail	-40°C	120°C	-32°C	112°C
Payload 2	ArduCam	-20°C	65°C	-12°C	57°C
GPS	Skytraq	-45°C	85°C	-37°C	77°C

5.6.1.2 Internal Heat Source

The major internal heat source is due to the operation of the electronic components inside the satellite. Table 4 illustrates the power budget of each component obtained from the EPS (electrical power system) under different states.

Table 4 Internal heat generation of different components.

	OBC	EPS	ADCS	GNSS	TT&C				Payload		Total
	OBC100	EPS100	ADCS-10m	Orion B16-C1	TX	RX	Beacon	Antenna	ArduCAM	Deployed -Motor	
Nominal Mode (W)	1.5	1.1 (0.367*3)	2 (1*2)	-	0.42	0.48	0.0288	0.04	0	0	6.18
Volume (m^3)	1.232e-5	PDU: 1.088e-5 PCU: 1.088e-5 BMU: 1.088e-5	1.248e-5		1.344e-5			5.487e-5	-	-	-
Internal heat generation (W/m^3)	121753	33701 per board	80128 per board		69107			729	-	-	-

5.6.1.3 External Heat Source

There are three main external heat sources in space, Direct solar radiation, Albedo and Earth IR. In Figure 31 shows the relation between these three external heat sources.

Figure 32 The relative positions of the external heat sources and the satellite

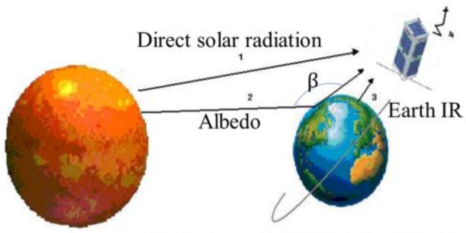

(1) Direct Solar Radiation

The equation of direct solar radiation can be expressed as follows,

$$I_{s,i} = I_s \cos\theta_i \tag{30}$$

where, $I_{s,i}$ is the solar radiation flux on each surface, I_s is the solar radiation flux which is a constant around 1400W/m^2 and θ_i is the angle between the surface's normal vector and the sun vector. If the value of cosθ_i is negative, the sun light is not contact the satellite directly and the direct solar radiation is set to be 0. So as when the satellite passes through the shaded area of the earth.

(2) Albedo

Albedo is the heat flux that from the sun and reflected by the earth, its equation can be written as,

$$I_{a,i} = I_s\gamma F\cos\beta \tag{31}$$

where, $I_{a,i}$ is the albedo radiation flux on each surface, γ is the earth albedo which varies with latitude and the reflecting substance but averaging the whole earth will be 0.3, F_i is the view factor of each surface to earth and β is the angle between sun-earth vector and earth-satellite vector.

(3) Earth Irradiation

The equation of earth irradiation (Earth IR) is as follows,

$$I_{e,i} = I_e F_i \tag{32}$$

where, $I_{e,i}$ is the earth radiation flux on each surface, I_e is the earth radiation flux which is constant around 213 W/m^2.

5.6.1.4 View Factor

Rickman (Rickman, S. L. 2002). had developed a method to calculate the view factor between the spheric earth and the non-spheric satellite. Which can be expressed as below,

$$\begin{cases} F_{\parallel} = \left(\frac{r_e}{r_e+h}\right)^2 \\ F_{\perp} = \frac{1}{2\pi}\left[\pi - 2\sin^{-1}\left(\sqrt{1-\left(\frac{r_e}{r_e+h}\right)^2}\right) - \sin\left(2\sin^{-1}\left(\sqrt{1-\left(\frac{r_e}{r_e+h}\right)^2}\right)\right)\right] \end{cases} \quad (33)$$

where, $F_{/\!/}$ is used for the parallel surface of the satellite when the earth is viewed as a flat plan, r_e is the radius of earth, h is the satellite's altitude and $F_{\perp}$ is the used in surfaces that are vertical to the earth surface.

5.6.1.5 Extra External Heat Source During Decay

An additional external heat is considered during the decay due to the extremely high velocity of the CubeSat and the increasing of the atmospheric density as the altitude reduces. There will be shock wave at the nose region of the satellite which will generate shock heating or the so-called re-entry heat. The relation between the altitude of the satellite and its velocity can be expressed as,

$$v = \sqrt{\frac{GM}{R}} \quad (34)$$

where, G is the gravitational constant which is $6.674 \times 10^{-11}\ \mathrm{N \cdot m^2/kg^2}$, M is the mass of the earth which is 5.9724×10^{24} kg and R is the orbit radius.

A NASA technical report by Sutton and Graves (Sutton, Graves, 1971) offered an easier way to estimate the stagnation point heating rate under different gas mixture as below,

$$q = Kv^3\sqrt{\frac{\rho}{R_n}} \quad (35)$$

where, K is the Sutton-Graves coefficient, v is the velocity of the satellite, ρ is the atmospheric density and R_n is the nose radius of the satellite. Table 5 (McBee, 2012) shows the value of the Sutton-Graves coefficient for different plantes and gas mixtures, where M_i represents the molecular weight of each type of gas molecule. Here, K is a constant around 1.7623×10^{-4} for earth.

Since the nose area of the CubeSat is not a circular shape, the effective radius (Carna, Bevilacqua, 2019) can be expressed as,

$$R_{n,eff} = \frac{Min(W,H)/2}{0.28} \quad (36)$$

where, $R_{n,eff}$ is the effective nose radius, W is the satellite's width and H is its height.

Table 5 The value of Sutton-Graves coefficient for different planets and gas mixture.

Coeff. for equation			Mass fractions							
	M_i	K_i	Earth	Mars	Titan	Venus	Neptune	Jupiter	Saturn	Uranus
N_2	28.013	0.11	0.785	0.027	0.984	0.035				
O_2	31.999	0.12	0.215	0.001						
H_2	2.016	0.04					0.8	0.898	0.967	0.825
He	4.003	0.08					0.19	0.102	0.033	0.152
Ne	20.180	0.15								
Ar	39.948	0.15		0.016						
CO_2	44.010	0.12		0.956	0.016	0.965				
NH_3	17.031	0.1					0.01			0.023
CH_4	16.042	0.08								
$K*10^{-4}$			1.7623	1.8980	1.7407	1.8960	0.6719	0.6556	0.6356	0.6645

5.6.2 Thermal Analysis

The thermal analysis is conducted by ANSYS Transient Thermal modulus. The material properties of each subsystem component are derived from reference to CubeSat flight heritage. The following Tables and plot represent the input of the thermal simulation. The orbit is defined by the parameters listed in Table 6. The heat generation of each subsystem components are as Table 4 shows. The external heat flux of each surface of the satellite in an orbit is as illustrated in Figure 32 And 33 the additional external heat flux of each surface of the satellite during a portion of the decay process (320~250km).

Table 6 Sun-synchronized orbit

Perigee	Apogee	Inclination	Period	Semi major axis	RAAN
523.3 km	537.7 km	97.5	95.1 min	6901 km	200 deg

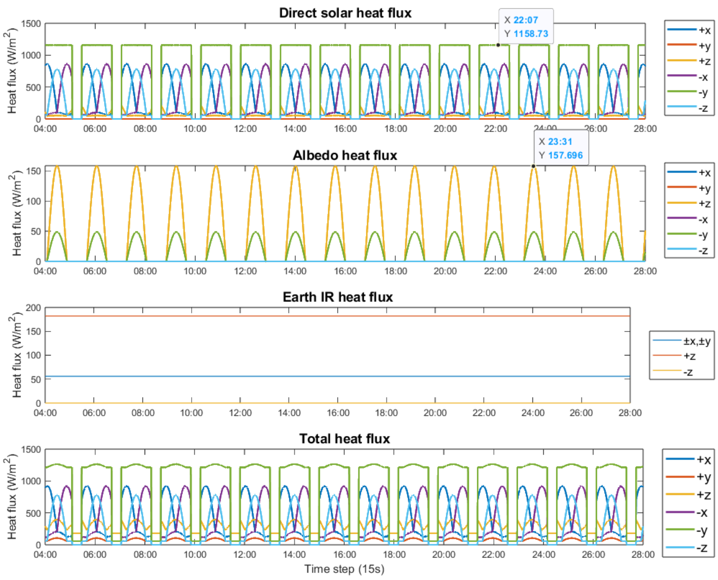

Figure 34
The external heat source in an orbit.

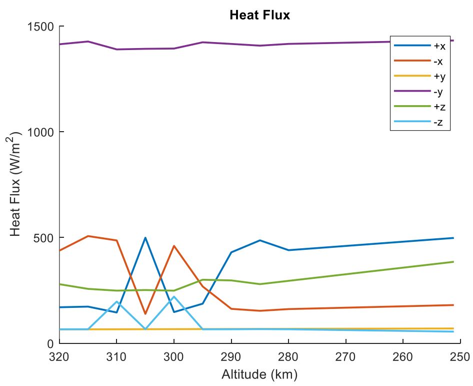

Figure 35 The additional external heat source of each surface of the satellite during decay.

5.6.3 Transient Thermal Simulation Results

For analysis cases, only the extreme cases are considered that are the hottest and the coldest case. The heat flux values were assigned every 15 seconds, covering a total simulation duration of 28,800 seconds. The outer radiation setting was based on the properties of anodized aluminum 6061-T6, with an emissivity of 0.76 (Hsieh, 2009). Radiation was modeled as occurring to ambient space at temperature of -270°C (3K).

5.6.3.1 Transient Thermal Simulation in the orbit

Figure 34 and 35 shows the simulation result of the coldest and the hottest case. Where, the minimum temperature of the cold case is -44.53°C and the maximum temperature of the hottest case is 81.27°C. Comparing to Table 1, most of the components will be in their working temperature through the orbit.

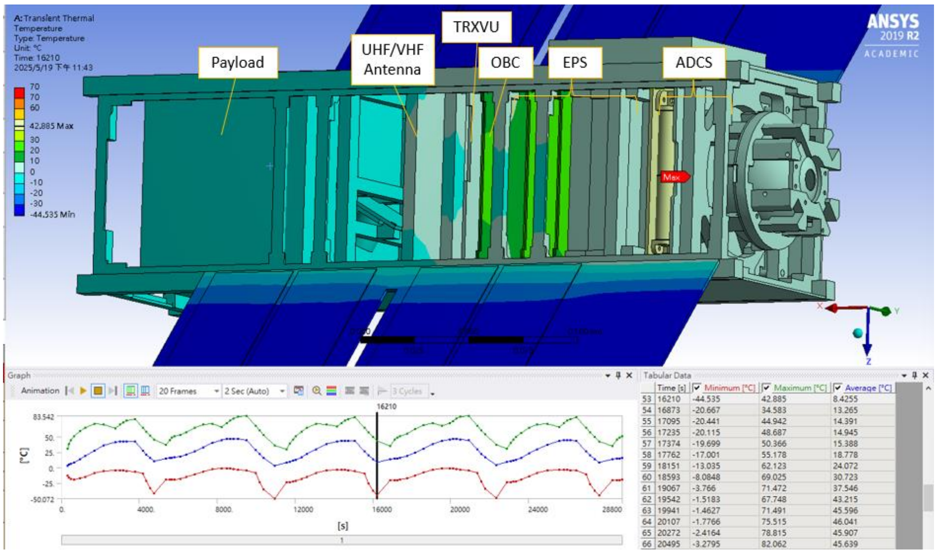

Figure 35 The internal transient thermal simulation of the satellite in an orbit cycle under the coldest case.

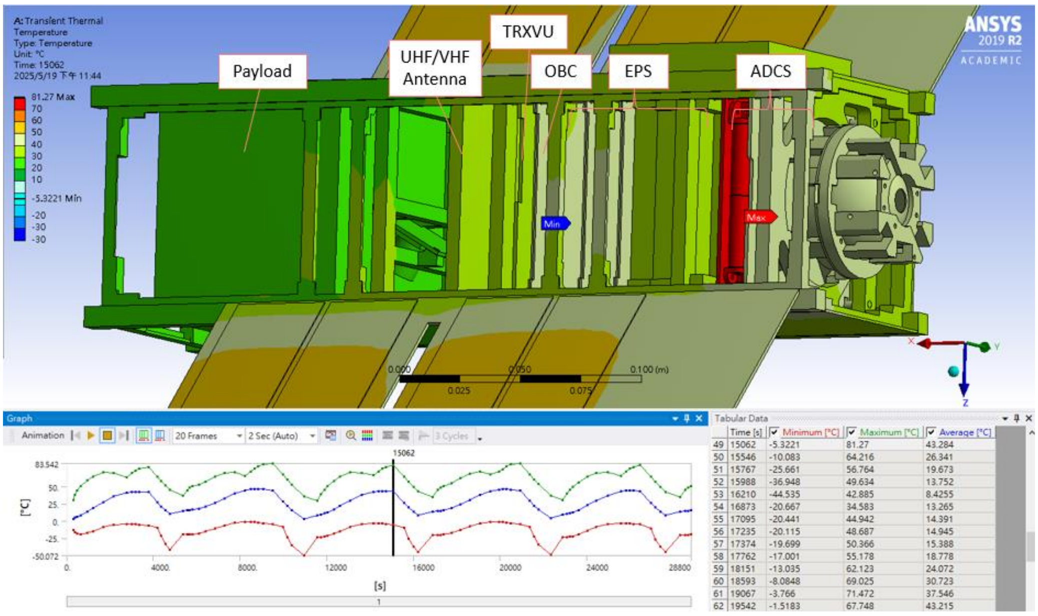

Figure 36

The internal transient thermal simulation of the satellite in an orbit cycle under the hottest case.

Table 8 The values of the thermal simulation results of each subsystem.

Case:		In main orbit (~550 km, RAAN=200 deg)	
		Min (℃)	Max (℃)
OBC		25	45
EPS		5~25	35~45
ADCS		5~42.9	35~81.3
TT&C	Board	5	35
	Antenna	5	35
Payload Deployed Mechanism		-5	25
Solar Panels &Cells		-44.5 (min)	55 (max)

5.6.3.2 Transient Thermal Simulation during decay

Figure 36 represents the temperature distribution of each subsystem due to the additional external heat flux. This simulation shows that most of the components of the satellite are under their operating temperature.

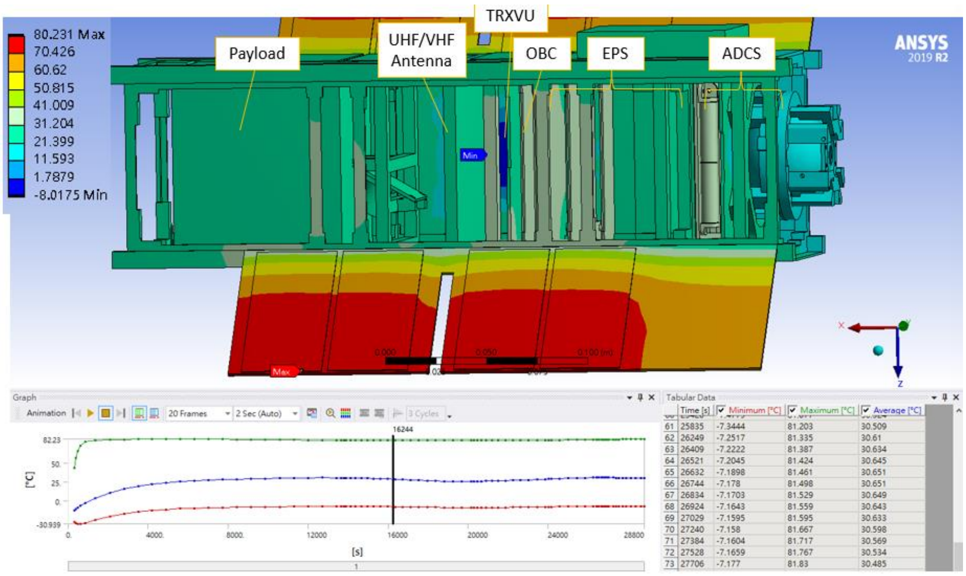

Figure 37 The transient simulation result of additional external heat source.

The transient thermal simulation results show that the CubeSat can survive under the space environment under our passive thermal coating. As decay mode begins, external heat sources fluctuate as SATEBAL moves through lower orbits, impacting its heat distribution, especially the solar panels. The mission ends when SATEBAL reaches approximately 200 km, the start of the thermosphere, where it burns up due to friction with dense atmospheric particles. This process ensures that SATEBAL fully disintegrates, aligning with its objective of complete deorbiting.

6. Conclusion

This study presents the design, implementation, and validation of SATEBAL. This CubeSat mission integrates a semi-passive attitude stabilization strategy with a controllable deployment mechanism. The mission demonstrates a novel approach to satellite stabilization by utilizing a variable-inertia system composed of deployable booms and tip masses, effectively enabling gravity-gradient-based attitude control. By optimizing the principal axes of the satellite's inertia matrix, the system achieves passive equilibrium orientation without relying on continuous actuation.

Complementing this stabilization strategy, an active control system based on magnetorquers ensures robustness against environmental disturbances, as validated through Lyapunov-based stability analysis. In the final mission phase, a deployable drag sail is used to enhance aerodynamic drag, ensuring compliance with space debris mitigation guidelines by accelerating orbital decay. Comprehensive aerodynamic modeling, incorporating both Free Molecular Flow and Response Surface Methodology, confirms the drag sail's effectiveness and provides accurate lifetime predictions.

The successful integration of deployable mechanical systems with hybrid control architectures, along with subsystem-level validation via simulation and ground testing, establishes SATEBAL as a promising platform for future small satellite missions requiring energy-efficient stabilization and responsible end-of-life disposal.

7. Reference

Acero, I. F., Diaz, J., Hurtado-Velasco, R., Bautista, S. R. G., Rincón, S., Hernández, F. L., ... & Gonzalez-Llorente, J. (2023). A method for validating CubeSat satellite EPS through power budget analysis aligned with mission requirements. *IEEE Access, 11*, 43316–43332.

Bak, T., & Wisniewski, R. (1997). Passive aerodynamic stabilisation of low Earth orbit satellite. In B. Kaldeich-Schuermann (Ed.), *Spacecraft guidance, navigation and control systems: Proceedings of the 3rd ESA International Conference, 26–29 November 1996, ESTEC, Noordwijk, the Netherlands* (ESA SP-381, p. 469). European Space Agency.

Carna, Bevilacqua. (2019). High fidelity model for the atmospheric re-entry of CubeSats equipped with the drag de-orbit device. *Acta Astronautica, 165*, 448–462.

Fiorillo, F., Santoni, F., Ferrara, E., Battagliere, M. L., Bottauscio, O., & Graziani, F. (2010). Soft magnets for passive attitude stabilization of small satellites. *IEEE Transactions on Magnetics, 46*(2), 670–673.

Fischell, R., & Mobley, F. (1964). A system for passive gravity-gradient stabilization of Earth satellites. *Guidance and Control Conference*.

Hsieh, Y. H. (2009). *Analysis and design of the nano-satellite thermal control subsystem* [Master's thesis, National Cheng Kung University].

Hughes, P. C. (2012). *Spacecraft attitude dynamics*. Courier Corporation.

Kumar, R. R., Mazanek, D. D., & Heck, M. L. (1995). Simulation and Shuttle Hitchhiker validation of passive satellite aerostabilization. *Journal of Spacecraft and Rockets, 32*(5), 806–811.

Lee, T. (2011). Geometric tracking control of the attitude dynamics of a rigid body on SO(3). In *Proceedings of the 2011 American Control Conference*.

Majid, A., Owais, M. N., & Qureshi, M. N. (2018). Aerodynamic drag computation of Lower Earth Orbit (LEO) satellites. *Journal of Space Technology, 8*(1), 82–89.

McBee. (2012). *Spacecraft reentry heating plugin*. Analytic Graphics Inc.

Mehta, P. M., Walker, A., Lawrence, E., Linares, R., Higdon, D., & Koller, J. (2014). Modeling satellite drag coefficients with response surfaces. *Advances in Space Research, 54*(8), 1590–1607.

Moe, K., & Moe, M. M. (2005). Gas–surface interactions and satellite drag coefficients. *Planetary and Space Science, 53*(8), 793–801.

National Aeronautics and Space Administration (NASA). *Solar cycle progression and forecast*.

Psiaki, M. L. (2004). Nanosatellite attitude stabilization using passive aerodynamics and active magnetic torquing. *Journal of Guidance, Control, and Dynamics, 27*(3), 347–355.

Rickman, S. L. (2002). A simplified, closed-form method for screening spacecraft orbital heating variations. In *11th Thermal and Fluids Analysis Workshop* (No. JSC-CN7458).

Shuster, M. D. (1993). A survey of attitude representations. *Navigation, 8*(9), 439–517.

Space Exploration Technologies Corp. (SpaceX). (2021). *Falcon user's guide*.

Spencer, D. A., Betts, B., Bellardo, J. M., Diaz, A., Plante, B., & Mansell, J. R. (2021). The LightSail 2 solar sailing technology demonstration. *Advances in Space Research, 67*(9), 2878–2889.

Sutton, G. P., & Graves, R. D. (1971). *A general stagnation-point convective-heating equation for arbitrary gas mixtures*. NASA, Hampton, VA.

Tensor Tech. *Magnetorquers*. https://tensortech.co/product/category/mtq

Tsuruda, Y. (2014). *Introduction to CubeSat power control system* (KiboCUBE Academy Lecture 08). Department of Aerospace Engineering, University of Tokyo NESTA.

Vinh, N. X., Busemann, A., & Culp, R. D. (1980). *Hypersonic and planetary entry flight mechanics*. NASA STI/Recon Technical Report A, 81-16245.

Walter, U. (2018). *Astronautics: The physics of space flight* (3rd ed.).

Wang, Y., & Xu, S. (2013). Gravity gradient torque of spacecraft orbiting asteroids. *Aircraft Engineering and Aerospace Technology, 85*(1), 72–81.

Wiesel, W. E. (1989). *Spaceflight dynamics*. McGraw-Hill.

Wilkie, K. (2021). The NASA advanced composite solar sail system (ACS3) flight demonstration: A technology pathfinder for practical smallsat solar sailing.

Yakovlev, M. (2005). The "IADC space debris mitigation guidelines" and supporting documents. In *4th European Conference on Space Debris*.